Graphene Field-Effect Transistors on *p-doped* Semiconductors for Photodetection

Nusrat Jahan

Thesis submitted to the faculty of the Virginia Polytechnic Institute and State University
in partial fulfillment of the requirements for the degree of

Master of Science
in
Physics

Nguyen Q. Vinh, Chair
Jean J. Heremans
Michel Pleimling

August 21, 2024

Blacksburg, Virginia

Graphene Field-Effect Transistors on *p*-doped Semiconductors for Photodetection

Nusrat Jahan

ABSTRACT

Recent advancements in photodetection using 2D materials suggest significant improvements in the performance of photodetectors. Among these, graphene field-effect transistors (GFETs) have demonstrated promising enhancements in photodetection, characterized by low noise, broad-spectrum response, high responsivity, and fast response [46, 126]. These photodetectors utilize graphene as the active channel, with graphene deposited on an insulating layer and semiconductor substrate. The contact of graphene with an insulator/semiconductor structure induces an interfacial potential to trap one type of photo-generated carrier at the interface. The trapped charge carriers induce opposite carriers in the graphene channel through the capacitive coupling effect. Due to a long lifetime of trapped carriers, the induced carriers in the graphene channel circulate multiple times under a given bias between the source and drain contacts, generating a photocurrent with high gain. Here, we explore GFET photodetectors fabricated on *p*-GaAs and *p*-Si wafers at room temperature. The photodetectors achieve a high gain. The photocurrent is generated due to the photogating effect.

In this work, we explore GFET photodetectors fabricated on *p*-GaAs and *p*-Si wafers at room temperature. The photodetectors achieve a high gain and high responsivity of 10^6 (A/W) under the above bandgap excitation and can detect light below the bandgap illumination for both *p*-doped substrates. NEP and D* values of these detectors have been characterized along with response time characteristics. The NEP and D* values for both detectors are around 10^{-15} W/$\sqrt{Hz}$ and 10^{12} Jones respectively, indicating a sensitive photodetection. The response time characterization suggests the rise and decay time depends on incident power. These results provide us with a deeper insight into the photodetection of the GFETs from the ultraviolet to near-infrared region.

Graphene Field-Effect Transistors on *p*-doped Semiconductors for Photodetection

Nusrat Jahan

GENERAL AUDIENCE ABSTRACT

Photodetectors have numerous applications in our daily lives, such as optical sensors in mobile phones, telecommunications, and biological imaging. However, current photodetection technologies often struggle to meet the increasing demands of modern equipment. These technologies require improving the existing photodetectors so that they can operate at exceptionally high speeds with low noise. Graphene is a highly sensitive material, that has shown significant potential for photodetection due to its fascinating optoelectronic and mechanical properties. In this study, we fabricated two field effect transistors on two semiconductor materials of different bandgaps with a single layer of graphene added on top of the substrate/insulator layer for photodetection. Specifically, we investigate the performance of GaAs and Si substrates to understand how varying the substrate can affect photodetection so that it can open up possible routes to future applications.

Acknowledgments

I would like to express my sincerest gratitude to all the people who have helped me, guided me, shared ideas, and supported me in my academic pursuit.

First, I would like to thank my supervisor Dr. Vinh Nguyen for supporting me and allowing me to work in his lab. He was always open to discussing and sharing ideas for any problems I had during my research. At the same time, he guided me to look more and gain deeper insight in my research. I am always learning new ways to think and enhance my knowledge. I cannot thank him enough for all his support. I also appreciate the lab environment he created for us where we all work equally supporting each other.

I would like to extend my sincere gratitude to my lab mates Kalani Ellepola, Tharindu Rajapaksha, Leslie Howe, and Jiarong Cui. I am especially grateful to Dr. Yifei Wang, who graduated in Spring 2022. As my first mentor in this research, she was incredibly supportive and always willing to help with any questions I had. I deeply appreciate her wise advice and our friendly conversations.

My thanks also go to Leslie Howe for her constant support. She always helped whenever I needed her. I am particularly grateful to my close colleagues and friends, Kalani and Tharindu, with whom I have thoroughly enjoyed collaborating, whether on coursework problems or research challenges. Finally, I want to thank Jiarong for his invaluable advice and ongoing assistance. I also appreciate the hard work of the undergraduate researchers in our lab: Brady Talbert, James Li, Kinley Koch, Nick Swetz, and James Mason.

I am grateful to my committee member Dr. Jean Heremans for all his support. I also thank Dr. Michel Pleimling for being on my committee and supporting me.

I would like to express my appreciation to Dr. Camillo Mariani, the director of the graduate program, for his continued support. I would also like to thank Dr. Uwe Tauber and Dr. Mark Pitt for all their support. Additionally, I offer my sincere thanks to Betty Wilkins, our graduate program

coordinator, for her time, kind words, and diligent handling of all my official documents and requests.

I want to extend my deepest gratitude to my husband, Mehran Islam. His unwavering support, care, and dedication during my times of need have been invaluable. Words cannot fully express my appreciation for everything he has done for me.

I would like to express my heartfelt gratitude to my younger sister and brother. They are a constant source of joy and motivation, inspiring me to grow and become a more responsible and caring older sibling.

I want to express my heartfelt gratitude to my in-laws. I deeply appreciate your support and encouragement as well. Your confidence in my aspirations is highly appreciated.

Finally, I want to express my heartfelt gratitude to my parents. Your belief in me has been a constant source of motivation, providing the strength and determination I needed to persevere. I am deeply thankful for your love, sacrifices, and the countless ways you have supported me. Your faith in my aspirations has shaped my path and empowered me to reach for my dreams.

Nusrat Jahan

Blacksburg, Virginia

Thesis Outline

Chapter 1

List of Figures

List of Table

Chapter 1

Introduction

This section introduces photodetectors and fundamental theories to understand the thesis work. In section 1.1 the different types of photodetectors and their working principle are discussed. Section 1.2 overviews relevant theories of graphene in photo detection and the graphene-based photodetector. Section 1.3 discusses the performance parameter of photodetectors and lastly, section 1.4 discusses the present state of photodetectors along with points of improvement and the scope of our research.

1.1 Introduction to Photodetector

The ability to sense light and convert optical signals into an electrical signal has found various uses including optical communication, remote sensing, LiDAR (Light Detection and Ranging), spectroscopy, medical imaging, and biological science. All these applications crucially depend on the efficient photodetection technology with minimal noise and broadband detection range. Numerous recent breakthroughs in the field of photodetectors have been made to boost its performance with broadband absorption capabilities, ultrahigh gain, sensitivity, low noise levels [1-3] and a lot of sectors for improvement are still a part of active research. Currently, there exist various photodetectors, which can generally be classified into two main categories in the commercial market: photon detectors and thermal detectors. Photon detectors function by detecting the interaction between incoming photons and the detector material, whereas thermal detectors measure temperature changes caused by the absorption of incident radiation. Based on their interaction with incident photons the photon detectors can be further categorized and the most widely used photodetectors are photoconductor and p-n junction photodiode.

1.1.1 Photoconductor

In photoconductors, a semiconductor is used as an active channel with two ohmic contacts to connect terminals with an external voltage circuit (Figure 1.1). When a semiconductor absorbs a photon with energy greater than its bandgap, an electron situated in the valence band absorbs this energy and moves to the conduction band. This process generates electron-hole pairs, where

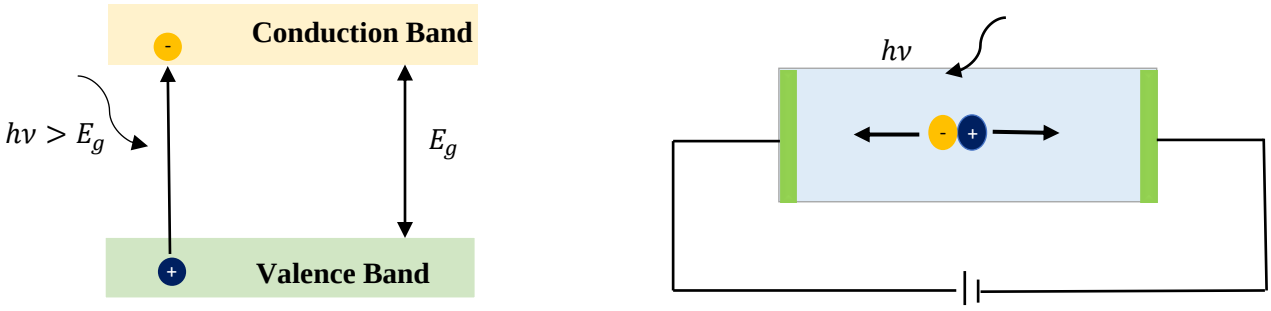

Figure 1.1: Working principle of a photoconductor a) Band diagram showing the generation of an e-h pair after irradiation of $h\nu > E_g$ is incident on absorbing material and b) An e-h pair is generated under irradiation and separated by an applied voltage, generating a photocurrent.

electrons are moved to the conduction band and holes remain in the valence band. The pairs of e-h can then be separated with an applied voltage, resulting in a photocurrent. The photocurrent varies significantly based on the energy of incident photons. When the energy of photon is lower than the bandgap of the absorbing material, electrons in the valence band cannot acquire sufficient energy to transit to the conduction band. Consequently, the material remains transparent to the incident radiation. The bandgap of the material, E_g, and incident photon wavelength, λ_{inc} is related by,

$$E_g = \frac{hc}{\lambda_{inc}}, \qquad (1.1)$$

where c is the velocity of light, h is Planck's constant, λ_{inc} is the incident photon wavelength. Equation (1.1) shows that the absorbing material can only detect photons with a certain wavelength corresponding to the specific bandgap. For example, GaAs material having a bandgap energy of 1.42 eV can only detect photons with wavelengths shorter than 870 nm while Si with a bandgap energy of 1.11 eV cannot detect radiation with the wavelength longer than 1110 nm.

1.1.2 Photo Multiplier Tube

Photomultiplier tubes (PMTs) are highly sensitive detectors used to amplify low-level light signals into measurable electrical currents which can detect light from ultraviolet (UV) to near infrared (IR) wavelengths. The basic construction of a photomultiplier tube involves an optical window, photocathode, focusing electrode, electron multiplier (dynodes) and anode sealed in a vacuum

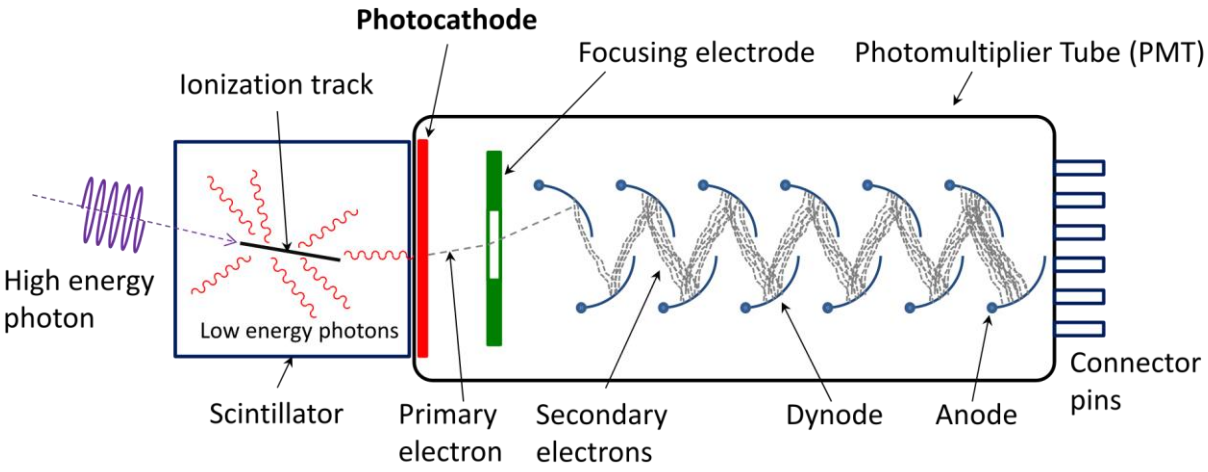

Figure 1.2: Illustration of photomultiplier tube coupled with a scintillator to convert high energy photon into low energy photon which is used as the source for PMT detector. The input passing through photocathode emits primary electron and each dynode increases the number of electrons through secondary emission.

pump. As light passes through the optical window the photocathode gets excited and emits electrons into vacuum. These emitted photoelectrons are accelerated and multiplied through a series of dynodes, each one increasing the number of electrons through secondary emission. This cascading effect results in a significant amplification of the initial signal, enabling PMTs to detect extremely weak light signals with high sensitivity. Figure 1.2 shows PMT detector coupled with scintillator designed to detect gamma rays. The photocathode used in PMT is usually made of semiconductor material. Hence photodetectors are wavelength dependent. The other factors that affect the electron multiplication are the shape, design and the supply voltage of the electrodes to efficiently focus the primary photoelectrons toward the first dynode.

1.1.3 Photoionization

Photoionization detectors (PIDs) are advanced gas detection instruments widely used in industrial settings, emergency response scenarios, and environmental monitoring. These detectors operate based on the principle of photoionization, where high-energy UV light is directed onto a gas sample. When UV photons interact with gas molecules, they ionize the molecules, causing them to release electrons. These free electrons create an electric current, which can be measured and

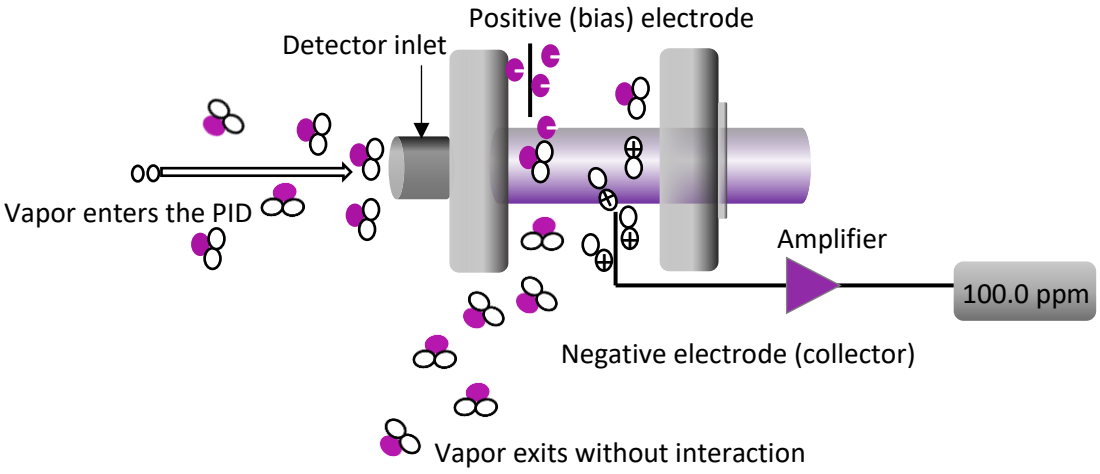

Figure 1.3: Schematic of photoionization detector. Gas molecules enter through the detector inlet and get ionized by an UV lamp. The ions are driven toward a collector electrode generating ion current. The current gets further amplified and converted by a digital meter to read in parts-per-million (ppm).

quantified to determine the concentration of gases present (figure 1.3). PIDs are particularly effective in detecting volatile organic compounds (VOCs) and other gases with low ionization potentials. They offer rapid response times, high sensitivity, and the capability to detect different types of chemicals.

1.1.4 Schottky Barrier Photodiode / *p-n* Junction Diode

The most widely used photovoltaic photodetectors are Schottky barrier diodes with metal-semiconductor-metal or *p-n* junctions, shown in Figure 1.4. Both photodiodes follow similar working principles based on the difference in work function at the junction. The work function representing the smallest energy needed for an electron to go into vacuum from a material does not change due to the metal-semiconductor contact. However, the difference in work function, φ, between the two materials leads to a discrepancy in the Fermi level, E_F induces the valence and conduction bands to bend. If the work function of the metal, $\emptyset_M$, is greater than *n*-type semiconductors, $\emptyset_S$, as shown in Figure 1.4 b, at the interface of the contact, electrons will transport from semiconductor to metal resulting in positively charged ions or a depletion region at the semiconductor interface.

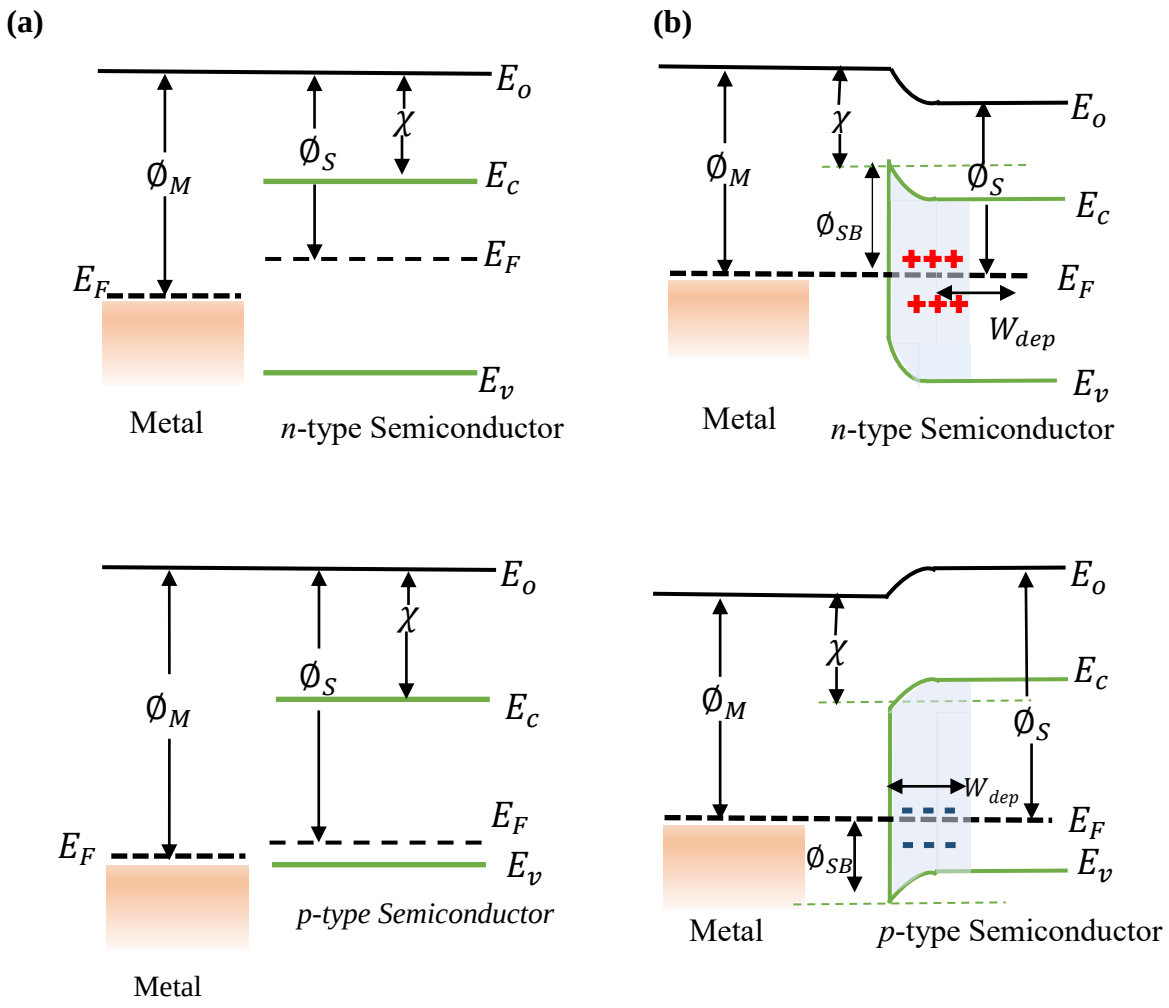

Figure 1.4: Schematic of a shottky or p-n photodiode a) Band illustration before contacting metal and n-type semiconductor b) Band illustration after contacting metal/n-type semiconductor (c) Band illustration before contacting metal and p-type semiconductor (d) Band diagrams after contacting metal/ p-type semiconductor.

As it happens the ions at the semiconductor interface cause the conduction and valence bands to bend upward (Figure 1.4 b) which in turn creates a built-in field. The internal field opposes any more charge transfer creating a potential barrier, named Schottky barrier, $\emptyset_{SB}$ [4]. This barrier helps to trap electrons in the metal side and prevents electrons from diffusing into other side. A similar situation is applied for metal/*p*-semiconductor contact. However, for *p*-type semiconductor-metal contact charge carriers are holes and if the work function of the p-type semiconductor is higher than the metal then holes will transport from the semiconductor to metal side, creating a depletion region with negative charged ions at the interface in Figure 1.4 d. The

depletion region at the junction can get wider or narrower depending on the external bias voltage. For the Schottky diode, when photons having higher energy than the bandgap of the material are absorbed, more e-h pairs in semiconductor are generated. The built-in field then separates the electron-hole pair in semiconductor; one of the charge carriers goes on the metal side, other stays trapped in semiconductor giving rise to a higher photocurrent than dark. Since the photodiode operates based on the built-in field it can be a self-powered device. However, the drawback of current photodiode technology is that it has low gain and low responsivity.

1.1.5 Thermal Detector

In the thermal detector, the incident radiation causes an increase in temperature. The temperature change induces a change in electrical resistance or internal polarization. The most widely used thermal detectors are thermopiles, microbolometers, and pyroelectric detectors. Thermopile and thermocouple detector measures radiation by utilizing the thermoelectricity principle to produce electricity by sensing the temperature (Seebeck effect), in which under a temperature gradient a voltage is generated across a circuit. Unlike single thermocouples, a thermopile comprises multiple thermocouple junctions linked together in series or parallel to enhance the produced voltage. This arrangement increases sensitivity and allows for more accurate temperature measurements. Although thermopile detectors are not very sensitive it still finds extensive use in various applications such as infrared thermometers, gas sensors, and thermal imaging cameras due to their reliability and low cost.

In comparison, bolometers are essential devices for detecting electromagnetic radiation based on changes of resistance, particularly in the infrared spectrum. They typically consist of thin, blackened flakes or slabs exhibiting impedance that varies significantly with temperature. Bolometers can be categorized into several types, including metal, thermistor, semiconductor, and superconducting bolometers. Metal bolometers utilize the variation in electrical resistance of metals with temperature, whereas thermistor bolometers rely on the resistance changes of materials sensitive to temperature. Semiconductor bolometers exploit the semiconductor materials' properties, and superconducting bolometers operate based on conductivity transitions, where resistance undergoes dramatic changes across a transition temperature range.

Lastly, the pyroelectric detector operates based on the principle of generating a current in response to changes in structural polarization induced by incident radiation. It can be conceptualized as a

small capacitor with two conducting electrodes positioned perpendicular to the material's spontaneous polarization direction. When radiation strikes the detector, the polarization shifts, causing charge to accumulate on the capacitor and generating an electric current. The current's strength depends on factors like the material's temperature increase and its pyroelectric coefficient. However, to extract the signal effectively, it's necessary to chop or modulate the incident radiation. This modulation is crucial for separating the desired signal from background noise. Despite the limitations, pyroelectric detectors offer advantages such as customizable response speeds, making them valuable for applications requiring fast detection.

Since the working principle of any thermal detectors does not require the creation of an charge carrier the incident radiation energy is independent of bandgap energy [5]. The independence from bandgap energy makes thermal detectors versatile across a wide range of wavelengths, from ultraviolet to far infrared region, without the need for material-specific optimizations. Most of the thermal detectors reported in the literature have high response times from 0.4 ms to 100 ms and they are usually bulky [6].

Traditional photodetectors available in the market utilize semiconductors like silicon (Si), gallium arsenide (GaAs), indium antimonies (InSb), germanium (Ge), HgCdTe etc. for their ability to give reliable performance and established production technologies. However, their sensitivity, detection range, and detectivity can no longer meet the requirements needed for advanced applications. To tackle this significant challenge, researchers suggest on the adoption of two-dimensional (2D) materials, offering an opportunity for substantial market growth and significant socioeconomic impact. Among the various applications of 2D materials in optoelectronics, photo-detection graphene stands out as particularly promising due to its interesting properties discussed in the following section [7-15].

1.2 Fundamental Properties of Graphene

Graphene consists of a monolayer of carbon atoms arranged in a hexagonal lattice. Since the discovery of isolated graphene from graphite by Geim and Novoselov in 2004 [7], it has gained a huge attention because of its intriguing electrical, optical, mechanical, and thermal properties [8]. Recent progress in the field of photo detection utilizes the unique properties of graphene to make ultrafast devices with broadband spectrum detection from UV to terahertz range [9-15]. In this

section, relevant properties of graphene regarding photo detection and sensor applications will be discussed.

1.2.1 Electronic Properties

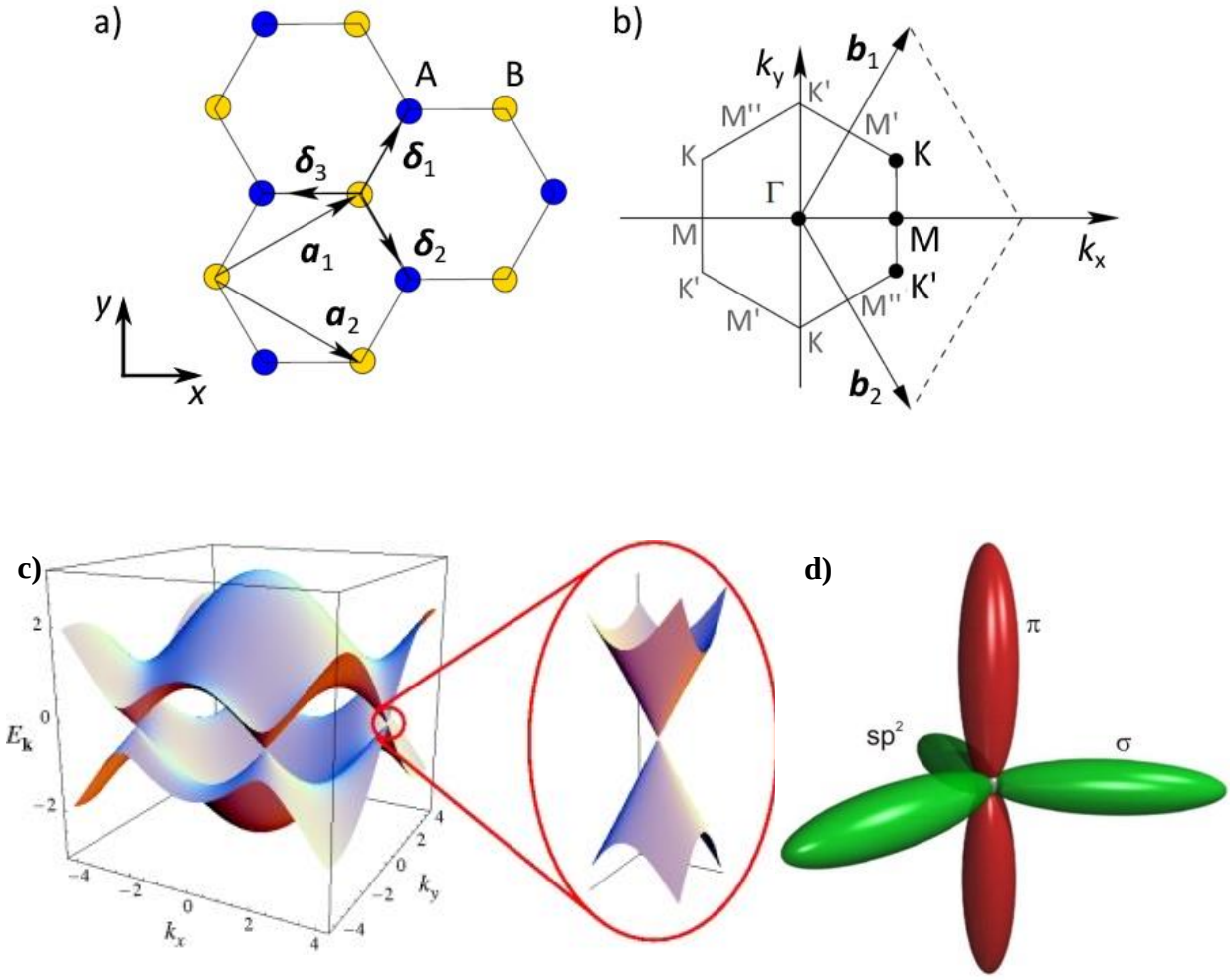

Figure 1.5: Lattice structure and Brillouin zone in graphene (a) Honeycomb lattice structure made out of two neighbouring carbon atoms with a_1, a_2, lattice unit vectors, and δ_i, the nearest neighboring vectors where i= 1, 2, 3 (b) The dirac cones are at k and k′ in Brillouin zone. [18] (c) Valence and conduction band of a single layer of graphene and one of the Dirac points shown by zooming in. (d) Schematic of sp^2 orbitals of one carbon atoms in graphene with π-electron [6] .

Graphene is made up of a single layer of carbon atoms and with sp^2 hybridization, it forms a honeycomb lattice with lattice constant, $a = 1.42\text{Å}$ (Figure 1.5 a). Each carbon atom has six electrons with two electrons in the inner shell and four in the outer shell or valence band. The four electrons in the valence band form sigma bonds with three neighboring carbon atoms in the two-dimensional structure, leaving one free electron in the third dimension. The three sigma bonds create a hexagonal structure giving the robustness and strength of graphene. A typical unit cell of graphene consisting of two carbon atoms referred to as A and B is shown in Figure 1.5. The free electron in π-orbital is called the π-electron and stays above and below the graphene sheet forming a π-bond. These π-bond create π and π^* bands in the valence and conduction bands, respectively, which control the conductivity of graphene. The dispersion relation which describes the energy of electrons with wave vectors, $k = [k_x, k_y]$ is established by using the tight-binding model [16, 17],

$$E(k) = \pm\gamma_o\sqrt{1 + 4cos^2\left(\frac{1}{2}ak_x\right) + 4cos\left(\frac{1}{2}ak_x\right).\cos(\frac{\sqrt{3}}{2}ak_y)}\ , \qquad (1.2)$$

where γ_o is the hopping energy between π-orbital to the nearest atom and a is the lattice constant. The valence and conduction bands therefore have different signs and the two bands touch at six points at k and k' points in the first Brillouin zone. The six points where the bandgap vanishes are called Dirac points or charge neutrality points (CNPs). Since the conduction and valence bands have no gap at the Dirac point graphene is known as a zero bandgap, thus, graphene is considered to be a semimetal [18]. The most interesting property of graphene happens near the Dirac point where the energy dispersion relation is linear with wave vector given by,

$$E = \hbar v_F\sqrt{{k_x}^2 + {k_y}^2}\ , \qquad (1.3)$$

where, $\hbar$ is Planck's constant, v_F is the fermi velocity. The linear dispersion relation for graphene is analogous to that of a relativistic particle. As a result, carriers in graphene mimic relativistic particles and have zero effective mass (massless Dirac fermions) with high Fermi velocity, v_F, around 10^6 m/s [19]. The most remarkable properties of graphene that rise due to this linear dispersion are high carrier mobility and ballistic carrier transport, which refers to the movement of charge carriers through the material without scattering, akin to the behavior of light in an optical waveguide [20]. A free-standing graphene above a Si/SiO_2 gate electrode is found to have carrier mobility > 200,000 cm^2/Vs [21] which surpasses conventional semiconductors such as silicon (Si)

(μ ≈ 1400 cm^2⁄Vs), gallium arsenide (GaAs) (μ ≈ 6000 cm^2⁄Vs) [22], and indium antimonide (InSb) (μ≈78000 cm^2/Vs). This unique combination of properties makes graphene a promising material for various electronic and optoelectronic applications where high-speed, low-energy consumption, and high-frequency operation are desired such as ultrafast transistors, high-frequency amplifiers, and ultra-sensitive sensors [6,24]. However, for optoelectronic device fabrication, a graphene layer is integrated into a semiconductor substrate and introduces certain challenges associated with environmental exposure and impurity interactions. The presence of impurities, defects, or phonon scattering events within the graphene lattice can significantly reduce its carrier mobility and overall conductivity [25-30]. For example, the graphene mobility on SiO_2 is reduced by interfacial phonon scattering to 40,000 cm^2⁄Vs [6]. Furthermore, the addition of bilayer or multilayer graphene can introduce interfacial effects and defects, which can further impact the conductivity of the material.

Additionally, intrinsic graphene has a finite carrier concentration due to its zero-bandgap nature and the fermi level is exactly at the Dirac point. The finite carrier concentration gives rise to the lowest current. However, the carrier concentration can be changed by doping, adding a graphene layer, or applying bias voltage at the gate and these changes shift the Fermi level. In field-effect transistors with graphene acting as a conductive channel for carrier transport, the fermi level goes below the Dirac point for negative bias voltage creating many holes in the valence band. In contrast, for positive voltage, the fermi level shifts up from the Dirac point creating many electrons in the conduction band. This continuous tunability of charge carriers from hole to electrons allows control over carrier concentration, conductivity, and other electronic properties for specific device applications.

1.2.2 Optical Properties

Graphene exhibits fascinating optical properties owing to its unique two-dimensional structure and electronic band structure. Graphene absorbs light due to its zero-bandgap nature. It absorbs around 2.3% of incident light per atomic layer, regardless of wavelength, which corresponds to the fine-structure constant, πα ≈ 2.3% [32,33]. Thus, graphene is nearly transparent across a broad range of wavelengths, spanning from UV to terahertz (THz) regions [31].

The optical absorption in graphene induces two different types of optical transitions: *intra*-band and inter-band transitions (Figure 1.6). Both transitions depend upon the Fermi energy, E_F, and

incident photon energy, E_{ph}. In the regime where the Fermi energy of graphene is greater than half of the incident photon energy only intraband transitions are allowed. This is because interband transitions, which involve the excitation of electrons from the valence band to the conduction band, are prohibited by Pauli blocking when the Fermi energy lies above half the photon energy ($2E_F > E_{ph}$).

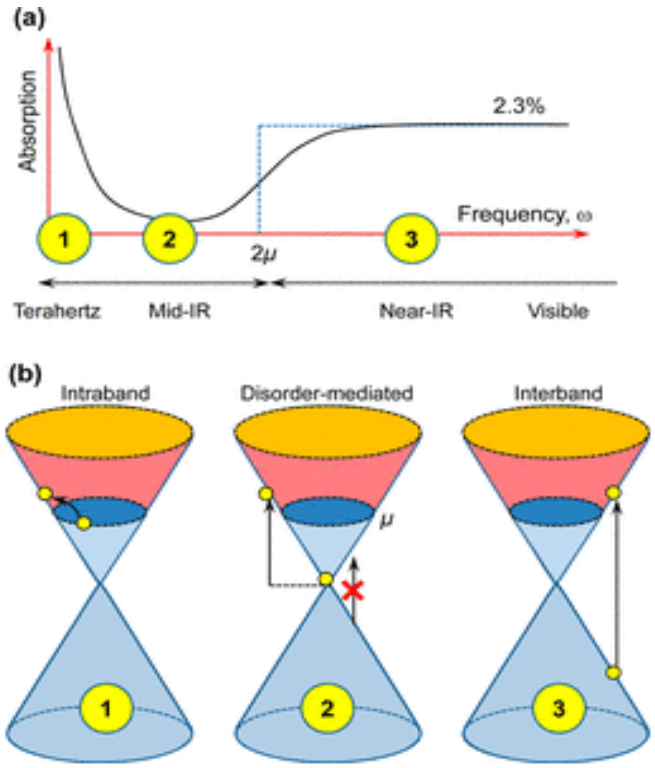

Figure 1.6: (a) Schematic of the absorption spectrum of graphene having a Drude peak at THz frequency, minimum absorption till mid-infrared region corresponding to Pauli blocking, and uniform absorption of 2.3% from near-infrared to visible range. (b) Illustrates intraband transition for incident energy less than E_F and interband transition at $2E_F \leq E_{ph}$ leading to uniform 2.3% absorption [6].

As a result, the low energy absorption from mid-IR to THz results in intraband transitions explained as Drude peak [34] while the high energy absorption from UV to IR leads to interband transition [31,35]. Since both the doping and bias voltage change the fermi level in graphene, the optical response can vary depending on these parameters. While it's impressive that a

monolayer graphene of just 0.4 nm thick, can absorb approximately 2.3% of incident photons [32], in comparison to the absorption seen in silicon with a thickness of 25 nm, this level of absorption remains relatively low for applications in light-sensitive devices like photodetectors and solar cells. To improve the absorption several approaches on adding a nanoparticle layer, Fabry-Perot microcavity [35], and photonic crystals [36], plasmonic effects [37-39] have been developed. The absorption spectrum can also be affected by substrate interaction and be wavelength-dependent [40].

1.3 Photocurrent Generation in Graphene-Based Detectors

Graphene's high carrier mobility, broad spectral absorption, and fast response time make it ideal for efficient light detection across a wide range of wavelengths and an excellent building block for hybrid photodetectors. Moreover, the tunability of graphene's electronic properties through doping or electrical gating allows for precise control over its photo-response characteristics, enhancing the performance and versatility of graphene-based photodetectors. Hence, it is important to understand the photo detection mechanism in graphene-based detectors. Out of many types of detection mechanisms, photovoltaic (PV) effect, photo-thermoelectric effect (Seebeck effect) and photo gating effect will be discussed.

1.3.1 Photovoltaic Effect (PV)

PV detectors (discussed in section 1.1.2) use the built-in electric field either between positively doped (p-type) and negatively doped (n-type) graphene, metal-graphene junction, or graphene Schottky junction to separate e-h pair. A bias voltage applied between the source and drain can generate the same effect by producing an external electric field. However, the latter case is used less as graphene is semi-metallic and an applied bias to the system creates a large dark current. The built-in electric field can be generated by chemical doping, applied gate bias, or using the difference in work function between graphene and metal contact. A typical phototransistor with a drain and source connected in short with a graphene channel is shown in Figure 1.7. Due to the difference in work function between graphene and metal, the e-h separates near the metal-graphene interface area, and an incident photon induces more e-h pair generating a photocurrent.

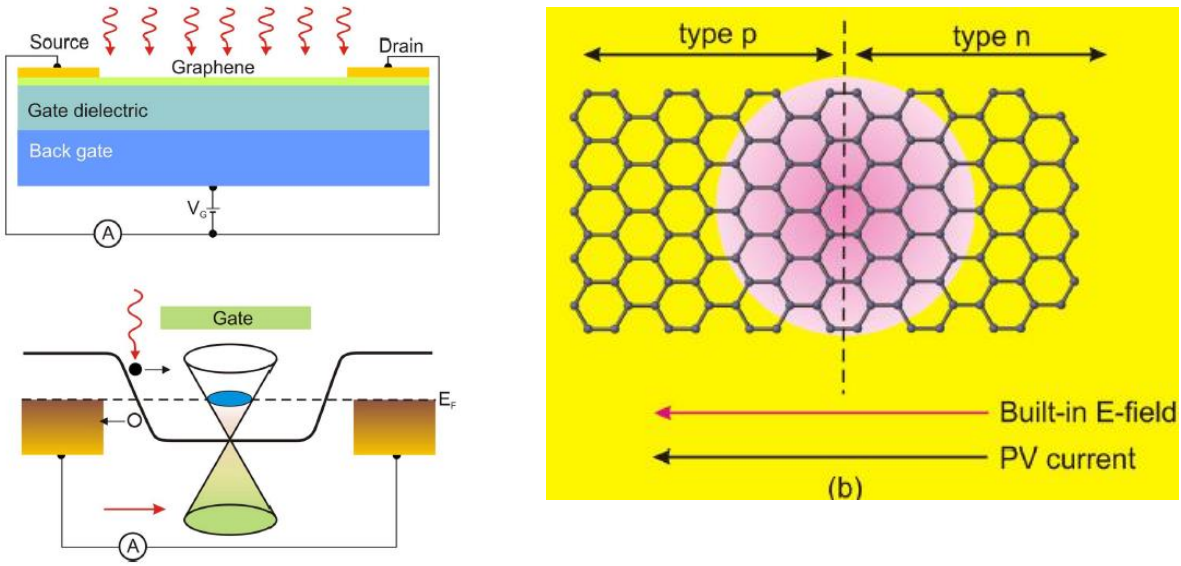

Figure 1.7: Graphene-based photodetectors (a) Schematic of a graphene-based phototransistor and photocurrent generation [6] (b) Illustration of the internal electric field and PTE effect of graphene p-n junction generating photovoltaic current from n-type to p-type [24].

In the middle of the graphene channel far away from any junction, there is no built-in electric field. However, at the junctions or interfaces where different materials interact with graphene, built-in electric fields emerges. As a result, photocurrent is zero in the middle while high photocurrent is observed near the contact.

1.3.2 Photo Thermal Electric Effect

The photothermal electric effect (PTE), also known as the Seebeck effect, is another significant mechanism contributing to photocurrent generation in graphene-based devices [41]. As the optical phonon energy is high in graphene (~200 meV), carriers generated by incident radiation remain at elevated temperatures compared to the lattice for an extended period (~ps). In response to incident radiation, localized temperature variations are induced within the material. This causes hot carriers, which are generated by the absorption of photons, to experience temperature gradients and subsequently diffuse throughout the material. The diffusion of hot carriers with different temperatures contributes to the generation of photocurrent within the device without the need for an externally applied bias. This characteristic enables zero dark current operation, meaning that

the detector doesn't produce a signal in the absence of incident light. The photocurrent (I_{ph}) can be related to the Seebeck coefficient through the following equation:

$$I_{ph} = (S_1 - S_2) \cdot \Delta T \cdot A \cdot \eta \qquad (1.4)$$

where, S_1, S_2 are Seebeck coefficients for different materials at the interface, ΔT is the temperature difference induced by incident light, A is the area of the detector and η is the efficiency of the photothermal conversion process. It's important to note that the Seebeck coefficient, *S*, depends on various factors such as the doping level of graphene, temperature, and material's properties. Therefore, controlling these parameters allows researchers to optimize the performance of PTE graphene detectors for specific applications.

1.3.3 Photogating Effect

Graphene photodetectors typically employ either graphene-metal junctions or graphene p-n junctions to spatially separate and extract photo-generated carriers. However, despite their potential, graphene-based photodetectors face significant challenges that hinder their performance in achieving high responsivity, ultrafast temporal response, and broadband operation. To overcome these issues and enhance performance in graphene-based photo detection, the photogating effect in field effect transistors (FET) has emerged as a well-utilized mechanism. In general, for FET the graphene layer (GFET), used as a channel between metal contacts (source and drain) is isolated from the substrate by an insulating layer. The work function difference at the insulator/substrate interface of GFET creates a potential well or built in potential. The photo generated e – h pair under illumination gets separated by the built-in potential and depending on the type of semiconductor either electron for *p*-type or holes for *n*-type accumulates at the substrate/insulator interface. As one type of carrier is trapped and insulating layer stays neutral, the opposite type of carrier is induced in graphene channel through capacitive coupling. When a voltage is applied at the source and drain, the holes or electrons in the channel move, generating current. If we consider a *p*-type semiconductor depending on the applied back-gate voltage, more and more carriers are pushed near the interface, generating a higher current. Due to the high mobility of carriers in the graphene channel and long lifetime of the trapped charge carriers, an ultrahigh gain is achieved in this process. A similar photo gating effect can also be seen using a top absorber layer on graphene. The absorber layer is used to overcome the limitation of only graphene detectors with low

responsivity of mA/W due to weak photon absorption [42-45]. In this case, e-h pairs are generated in the absorber layer and the difference in work function causes a potential well to trap one type of carrier in the absorber layer while the opposite type is induced in the graphene channel. The functionality of both the back-gated and top-gated photodetectors depends a lot on the material used. For back-gated detectors, the type of substrates with the same or different doping levels [46] can show interesting results which is the primary concern of this thesis. In contrast for the top-gated detector to increase photon absorption, different nanoparticles or quantum dots such as single-layer graphene/ZnO quantum-dot (QD) [47,48] have been utilized as an absorber layer with high responsivity. Overall, carriers trapped in graphene detectors can offer benefits such as enhanced responsivity, spectral sensitivity tuning, internal gain, and reduced dark current.

1.4 Figures of Merit for Detectors/ Performance Metrics for Photodetectors

Photodetectors play a critical role in modern optical and optoelectronic systems. Assessing the performance of these devices by parameters such as sensitivity, responsivity, and noise equivalent power, can provide valuable insights into the detector's performance across a wide range of applications [49,50]. In this section, we will discuss the performance metrics for a photodetector.

1.4.1 Photo Responsivity

Responsivity is a fundamental performance metric for photodetectors, quantifying their ability to convert an incident optical power into an electrical output. It is defined as the ratio of the generated electrical signal due to the incident photon to the optical power and is typically expressed in units of amps per watt (A/W),

$$R = \frac{I_{ph}}{P_{in}} = \frac{I_{light} - I_{dark}}{P_{in}} \ , \qquad (1.5)$$

where I_{ph} is the photocurrent which is the difference between the current due to incident light, I_{light}, and the current under dark conditions, I_{dark}, and P_{in} is the optical power incident on the detector. The power on the device is found from,

$$P_{in} = \varphi \frac{hc}{\lambda},$$

where φ is the number of photons per second at a certain wavelength, λ. The photocurrent that comes from the flow of electrons or holes is related to quantum efficiency, QE. The QE expressed

with η relates the number of charge carriers collected by a detector to the number of incident photons exceeding various external losses, including reflection, transmission, fast recombination, and so for a single photon the photocurrent with quantum efficiency can be written as $I_{ph} = \eta . q . \varphi$ with charge q. Relating all these, the responsivity can be found as

$$R = \frac{\eta q \lambda}{hc} \qquad (1.6)$$

A higher responsivity indicates that the photodetector produces a stronger electrical signal in response to a given amount of incident light, thereby offering increased sensitivity. Responsivity is influenced by various factors, including the detector's active area, material properties, optical wavelength, and operating conditions. Optimizing responsivity is crucial for enhancing the performance of photodetectors for specific applications.

1.4.2 Photoconductivity Gain

When an electron-hole pair is created in a graphene detector, one type of charge carriers can be trapped at the substrate/insulator interface due to interfacial potential and opposite type of carrier is induced in the channel due to capacitive coupling. When a bias voltage is applied between source to drain the carrier in graphene channel transits very fast and in order to maintain the charge neutrality as soon as one carrier reaches drain another electron is introduced to the channel by an applied voltage which transits with fast speed resulting in a photoconductive gain. The gain is related to the lifetime of the trapped charge carriers and transition time of the opposite charge carriers between the channel by,

$$G = \frac{\tau_{life}}{\tau_{transit}} = \frac{\tau_{life} . \mu . V_{bias}}{L^2}, \quad (1.6)$$

where τ_{life} is the lifetime of the trapped charge carrier, $\tau_{transit}$ is transit time of other type of carriers between source and drain contacts. $\tau_{transit}$ depends on the carrier mobility, μ, the bias voltage,V_{bias} , and the length, L, of the channel. As gain is achieved through photo gating effect the responsivity of the detector can be related with the gain by,

$$R = \eta . G . \frac{q\lambda}{hc} \qquad (1.7)$$

This linear relationship suggests that if the gain is higher, then responsivity increases.

1.4.3 Response Time

Response time is a critical parameter for photodetectors, reflecting how quickly the detector reacts to variations in incident light. It encompasses two key components rising and recovery times. The rising time measures the duration it takes for the photocurrent to increase from 10% to 90% of its final value when the device is exposed to illumination. Recovery time signifies the time it takes for the photocurrent to drop from 90% to 10% after the light source is removed. Shorter rising and recovery times are desirable for applications requiring rapid transitions. Therefore, response time directly impacts the photodetector's ability to track changes in light intensity, making it a crucial consideration in various optical and electronic systems

1.4.4 Noise Equivalent Power (NEP)

Photodetectors, like any other electronic device, are susceptible to various types of noise due to the movement of charge carriers within the device. These noise sources can degrade the signal quality and impact the sensitivity and performance of the photodetector. The major noise sources for photodetectors are categorized as thermal noise, shot noise, low frequency or $1/f$ noise, and generation-recombination (G-R) noise [51]. The combination of these unwanted signals or noises present in the output signal is a parameter of the detector's performance and it is characterized by the noise equivalent power (NEP). The NEP quantifies the smallest optical power that the photodetector can reliably detect above the noise level. In other words, NEP is the minimum detectable signal power that can be distinguished from the noise floor with a signal-to-noise (SNR) ratio of 1 in a frequency bandwidth of 1 Hz [52]. The NEP is represented in terms of power spectral density (PSD) of the different noises by,

$$NEP = \frac{Noise\ Current}{R_{ph}} = \frac{\sqrt{S_I(thermal)+S_I(Shot)+S_I(1/f)}}{R_{ph}}, \qquad (1.8)$$

where $S_I(thermal)$, $S_I(Shot)$, $S_I(^1/_f)$ are the spectral power density due to thermal noise, shot noise, and $1/f$ flicker noise respectively and R_{ph} is the photoresponsivity. NEP is typically expressed in terms of watts per root hertz (W/√Hz) or current per root Hertz (A/√Hz), depending on the type of photodetector. For a given photodetector, the NEP is typically lowest at the wavelength where the detector's responsivity is maximum. This is because higher responsivity implies that the photodetector can convert more of the incident optical power into an electrical

signal, thus improving the signal-to-noise ratio and reducing the NEP. To calculate the NEP, it is important to understand the different types of noises and their relation to the measurement. Therefore, in this section, the different noises will be discussed.

Thermal noise, also known as Johnson-Nyquist noise, is the most common noise in almost any electronic device. Thermal noise is caused by the random motion of charge carriers within the detector due to thermal energy. The power spectral density of thermal noise for current can be written using Nyquist relation as,

$$S_I(thermal) = {}^{4\,k_B T}/_{R} \qquad (1.9)$$

where k_B is the Boltzmann constant with unit joule/kelvin, T is the room temperature in kelvin and R is the resistance of the detector before applying light in **Ω**. The resistance unit can be converted to joule/ (second. Ampere^2). Therefore, the units for the current thermal noise is A^2/Hz. The relationship shows thermal noise is proportional to the temperature of the device and has a frequency-independent power spectral density.

Shot noise arises due to the discrete nature of electric charge and the random arrival of photons at the photodetector generating random fluctuations in the output signal. Shot noise is significant in low-light conditions and has a frequency-independent power spectral density. It is defined as,

$$S_I(Shot) = 2q.I_{dark} \qquad (1.10)$$

where q is the charge of the electron in coulomb and I_{dark} is the dark current in ampere. The unit for shot noise is A^2/Hz. The dark current is the leakage current that flows through the photodetector even in the absence of incident light. Dark current is caused by the thermal generation of electron-hole pairs within the detector material and contributes to the overall noise level of the detector. Both the shot noise and thermal noise correspond at high-frequency regions.

The presence of 1/f noise, also known as flicker noise, is a well-documented phenomenon observed in low-frequency regions. This low-frequency noise component, characterized by its inverse proportional relation to frequency, poses significant challenges in achieving high-performance photodetection systems. 1/f noise originates from a variety of sources, including fluctuations in carrier mobility, trap states within the semiconductor material, or interface effects [53]. The spectral density of 1/f noise can be expressed as [54,55],

$$S_I\left(1/f\right) = \frac{A.\ (I_{dark})^2}{f^{\beta}} \qquad (1.11)$$

where A is the noise amplitude of the device without light (dimensionless), f is the frequency at which the noise is measured, typically 1 Hz and β is the frequency component with a value near 1 [51,56]. The unit for 1/f current noise is A^2/Hz.

Lastly, the generation-recombination noise arises from fluctuations caused by the generation and recombination process of free charge carriers within the photodetector material. This noise dominates the noise level in the middle-frequency range and has a frequency-dependent power spectral density.

The combination of all these noises gives us the noise equivalent power (NEP) according to equation (1.8) with a unit of W/$\sqrt{Hz}$.

1.4.5 Specific Detectivity

Specific detectivity, denoted as $D^*$is the most important figure of merit for photodetection systems as it enables direct comparison among various detectors regardless of their active area and operating frequency. It quantifies the ability of a detector to distinguish a weak optical signal from the noise floor and is proportional to the reciprocal of the NEP. The formula to calculate D^* is given by,

$$D^* = \frac{\sqrt{A_{channel}}}{NEP} \qquad (1.12)$$

Where, $A_{channel}$ is the active area of the transport channel. The unit of D^* is cm $\sqrt{Hz}$ /W (Jones). Since, D^* is inversely related to the NEP, a higher D^* value indicates better sensitivity and performance, allowing for more accurate and reliable detection of faint signals above the noise level.

1.5 Present Status of Visible Range Graphene-Based Photodetectors and Our Research

Transforming light into electrical signals remains a state-of-the-art technology with widespread implications for various aspects of our daily lives, including optical communication, video imaging, medical imaging, spectroscopy, and more. From the broad-spectrum range the UV-visible range is most closely intertwined with our daily experiences. Numerous studies on visible

photodetectors reports using silicon, group III-V, and group II-VI semiconductors due to their exceptional performance, cost-effectiveness, maturity, and seamless integration with electronic systems. The two most widely used applications of photodetectors are complementary metal-oxide-semiconductor (CMOS) and charge-coupled device (CCD). CMOS sensors offer advantages such as lower power consumption, faster readout speeds, and potentially lower manufacturing costs compared to CCDs [57,58]. However, the present CMOS technology faces the limitations of high noise, low sensitivity, high manufacturing cost, and flexibility with certain semiconductor growth [59]. The limitations of CMOS sensors arise due to high carrier transit time in photodiodes, high dark current [60]. In this context, 2D materials, colloidal quantum dots (CQDs), and organic semiconductors have emerged as promising candidate platforms. Photodetectors based on CQDs have showcased notable attributes, including high photoconductive gain ranging from 10^3 to 10^6 A/W and detectivity reaching up to 10^{13} Jones (cm. $\sqrt{Hz}$/W) across the visible to shortwave-IR spectrum [61,62]. Out of many available 2D materials graphene shows itself as a promising building block for the photodetectors due to its fascinating properties described in section 1.2. The performance of graphene-based photodetectors from different literature is shown in Table 1 adapted from [63].

Table 1: Performance of graphene-based photodetectors in literature

Device	**Responsivity**	**Detectivity**	**Excitation Wavelength**	**Response time**	**Ref**
Gr/h-BN/ $MoSe_2$ and $Si/SiO_2/MoSe_2$	314 A/W	2.2×10^{12} Jones	532 nm	–	[64]
Si/SiO_2/Graphene/Gold nanoparticle	6.1 mA/W	–	514 nm	–	[65]
$(C_4H_9NH_3)_2PbBr_4$/Gr	2100 A/W	–	510 nm	–	[66]
PbS quantum dot and CVD-grown graphene	10^7 A/W	–	895 nm	–	[67]
graphene-PbS	10^7 A/W	7×10^{13} Jones	600 nm	10 ms	[68]
Graphene and Cu_2O based hybrid device	1.2×10^{10}A/W	1.4×10^{12} Jones	450 nm	–	[69]

Device	Responsivity	Detectivity	Excitation Wavelength	Response time	Ref
Dimethylamine-functionalized graphene quantum dots	10^4 A/W	10^{11} Jones	255 nm	1 s	[70]
$MoTe_2$/ graphene	970.82 A/W	1.55×10^{11}Jones	1064 nm	78 ms	[71]
graphene-black phosphorus	3.3×10^3 A/W	–	1550 nm	$T_r = 4$ ms	[72]
graphene-MoS_2 binary Heterostructure	5×10^8 A/ W	–	635 nm	$T_r = 1$s	[73]

Hybrid graphene–CQD phototransistors consisting of a single or bilayer graphene with a thin film of CQD's able to operate from UV to short-wave IR (SWIR) are reported to have responsivity of 10^7 A/W in the short-wave-IR range [68]. But the response time for the hybrid Gr-CQD is in millisecond time scale (~10 ms). Graphene integrated with other 2D material (MoS_2) is reported to exhibit a dual photo gating effect and very high responsivity of 5×10^8 A/ W in the visible range with a long recombination time ~1s [73]. In recent developments, hybrid detectors combining graphene with $MAPbI_3$ perovskite have demonstrated notable advancements. These detectors exhibit a responsivity of 10^7 A/W and a detectivity reaching approximately 10^{15} Jones with a slow response time (<1s) [74]. According to the reviewed literature, these photodetectors although have high gain still show slow response time which creates a barrier to the progress of visible-range photodetectors. Therefore, it is valuable to explore alternative strategies and find an optimum balance between high responsivity, low noise, and fast response time. In this thesis, we explored graphene field effect transistor (GFET) photodetectors on two widely used substrates: silicon (Si) and gallium arsenide (GaAs). Silicon is a widely used semiconductor with well-understood properties and established fabrication techniques. By combining Si with graphene, the resulting hybrid photodetector leverages the best of both materials [75-79]. Si-based graphene field effect transistors utilizing the photogating effect at the back gate are observed to have high gain, high responsivity, and fast response (<ns) [80]. However, Si-based technology can suffer from lower optical absorption due to an indirect bandgap of 1.12 eV and lower mobility ($\mu \approx 1400$ cm^2/Vs), whereas gallium arsenide (GaAs) has a direct bandgap (1.4 eV) and higher mobility ($\mu \approx 6000$

cm^2/Vs. Looking at the properties of Si and GaAs, they are quite competitive in terms of cost and performance and are used widely in photonic devices. Since photogating induced by substrate is less studied, by understanding the contribution of different substrates in the photo-gating effect, researchers can potentially unlock new opportunities to optimize GFET performance. Therefore, it is intriguing to investigate and compare the photo-gating effect in both materials. For this thesis, both Si and GaAs substrates were chosen with a slight *p*-doping and used as an efficient photon absorber.

In this work, to elucidate the effect of changing substrate from Si to GaAs a systematic investigation of the performance of GFET photodetector is carried out under light illumination from visible to near infra-red.

Chapter 2

Fabrication and Experimental Setup

This chapter discusses the fabrication process of graphene-based photodetectors in section 2.1 and the experimental setups to characterize the photodetectors in section 2.2.

2.1 Fabrication of Graphene Field Effect Transistor

To make graphene-based FET devices, three electrodes are needed to operate the device. The electrodes are the source, drain, and gate where the gate is insulated from the source and drains through a dielectric layer. The most used substrate for GFET is silicon with a SiO_2 insulating layer [84-88]. However, during the transfer process the carrier mobility of graphene reduces due to impurities and trapped charges in the SiO_2 surface [89]. Another competitive, low cost substrate for GFET fabrication is gallium arsenide (GaAs). Compared to Si, GaAs being, a group III-V material, has a higher energy gap (1.42 eV), higher mobility (6000 $cm^2V^{-1}S^{-1}$), and direct bandgap. These properties allow GaAs to be used for efficient photonic and electronic devices. However, GaAs does not have a native oxide like silicon and does not adhere to oxides well compared to the Si/SiO_2 interface [90]. One of the most studied and efficient dielectric layers for such group III-V material is silicon nitride (Si_xN_y) [91-95]. Because of the interesting properties of Si_xN_y such as high stability, low leakage, and high dielectric constant ~8, it was chosen as the insulating layer on GaAs substrate [96,97]. After growing the dielectric layer and metal contacts, a single graphene layer was deposited on the dielectric layer between the source and drain as a conductive channel to transport carriers. The carrier mobility in graphene is greatly reduced by the long-distance coulomb scattering [80-82]. A dielectric material, Ta_2O_5, with a high dielectric constant from 25-50, is reported in the literature to reduce the scattering in graphene as well as protect from atmospheric interaction [83,84]. Therefore, after growing the insulating layer, metal contacts and thin atomic graphene layer deposition on the insulating layer, a protective layer with Ta_2O_5 was grown on Si-GFET.

2.1.1 Fabricating Dielectric Layer

At the beginning of the fabrication process, GaAs and Si wafers used as the substrate of the device were etched using a buffer oxide etching (BOE) solution to remove the native oxide layer formed due to environment contact. After that, a 300 nm thick insulator layer with silicon oxide (SiO_2) was thermally grown on Si substrates using a furnace. For GaAs, a 300 nm silicon nitride was grown using plasma enhanced chemical vapor deposition (PECVD) at 350℃.

2.1.2 Fabricating Metal Contacts

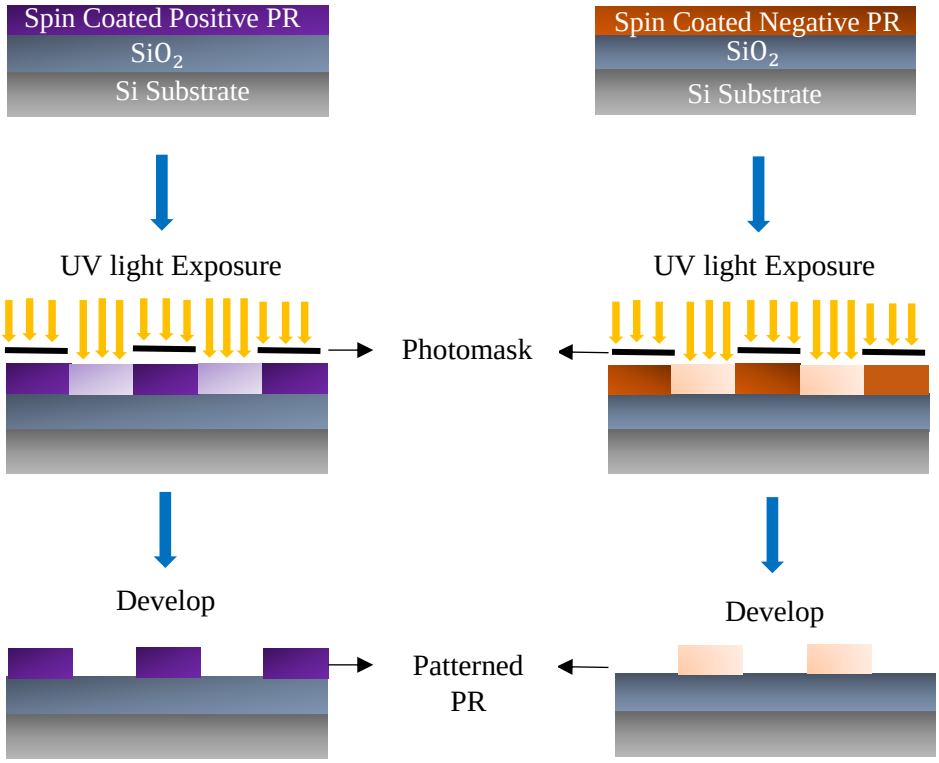

Figure 2.1: Illustration of patterning using positive and negative photoresist.

To make FETs, source, drain and back-gate contacts were made using photolithography. Photolithography is a technique for transferring geometric patterns from a mask to a substrate using light. First, a thin layer of photoresist material is deposited onto the substrate. The photoresist

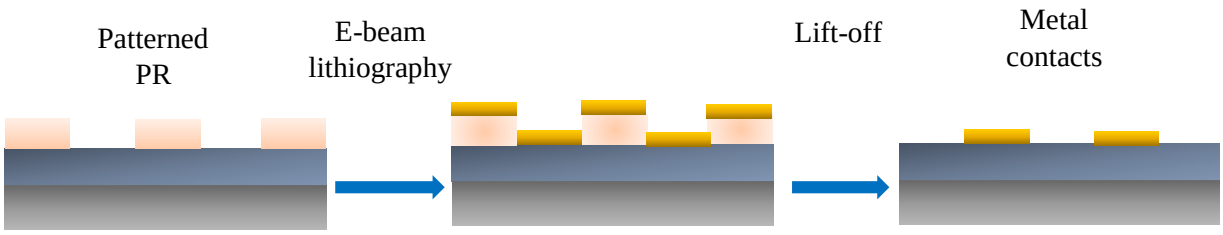

Figure 2.2: Fabrication of metal contacts on patterned photoresist layer.

is a light-sensitive material that undergoes chemical changes when exposed to light. Two types of photolithography processes including positive and negative photoresist are shown in figure 2.1.

Back Gate Contact Fabrication

To make a back gate a positive photoresist Shipley 1813 (S1813) was deposited at the center of the substrate and spin coated in two steps with 500 rpm for 10 sec and 2000 rpm for 30 sec (Figure 2.1). After the photoresist step the substrates were soft baked at 100℃ for 1 min. Then a photomask and Suss Mask Aligner MA6 were used to expose wafer with an ultraviolet lamp for 11 sec. After that the MIF 319 developer was used to develop features by dipping the wafers for 1 min. After that the wafer was submerged in buffered oxide etching for 4 min and cleaned with deionized (DI) water for 5 sec. In order to make the photoresist contact strongly, the wafer was heated for 1 min on a hot plate at 100 ℃. After these steps a geometrical pattern for the back gate contacts was produced. By using the electron beam evaporation deposition method with Kurt J. Lesker PRO Line PVD 250, titanium (Ti) and gold (Au) were deposited on the patterned location. After the deposition the wafer was immersed in acetone overnight. Due to dipping the wafer in acetone the sacrificial layer under Ti/Au is washed away. As a result, the Ti/Au film on the negative photoresist is lift off and only the Ti/Au touching the substrate remains. This makes it possible for the silicon or Gallium Arsenide wafer to work as the backgate. After the lift off the substrate was transferred in cleaned acetone for 1 hour, then dipped in isopropyl Alcohol for 30 min and DI water for 15 min. Lastly, the whole substrate was dried with nitrogen gas.

Source – Drain Contact Fabrication

For the source and drain contacts a negative photoresist Az nLOF 2020 solution was deposited, and spin coated (Figure 2.2). All the other steps of the fabrication were similar to the backgate formation except after exposing and developing the pattern no further etching is performed. The metal contacts with chromium (Cr) and gold (Au) were deposited directly on Si/SiO_2 and $GaAs/Si_3N_4$ insulating layers with PVD 250. After patterning, the wafer was submerged in acetone overnight and cleaned.

2.1.3 Cleaning the Photoresist Residue on Wafer

After the fabrication of metal contacts, the whole 4-inch Si/SiO_2 and $GaAs/Si_3N_4$ wafers are cut into square chips of 1 x 1 cm^2 by a dicing machine. Before dicing a 2 μm protective layer with positive photoresist S1813 is deposited on the whole wafer to protect metal contacts. After dicing the wafer into square chips they are cleaned again by dipping it in acetone for 1 hour, then transferred in isopropyl alcohol (IPA) for 30 minutes and finally immersed in DI water for 15 min. After cleaning nitrogen gas was used to dry the chips. The photoresist residue remains on the surface, and to remove that a reactive ion etching with by Samco RIE-10NR is employed with oxygen plasma operated at 30 W power, 10 sccm oxygen flow rate, and 30 mTorr pressure for 4 min.

2.1.4 Graphene Transfer

A single graphene layer grown by chemical vapor deposition (CVD) on copper foil (Cu) was purchased from Graphenea Inc. To transfer the graphene layer from Cu to the square chips a Poly (methyl methacrylate) (PMMA, MicroChem 450 A4 – (4.5% in anisole)) solution is first dropped on the Gr/Cu surface and spin coated on 1700 rpm (figure 2.3).

After spin coating the PMMA/Gr/Cu is kept in a vacuum chamber at 30 mTorr for 1 hour to dry. Then the copper foil is etched away by submerging the PMMA/Gr/Cu in 0.1M ammonium persulfate [$(NH4)_2S_2O_8$, Sigma-Aldrich, ≥ 98%] for 1 hour 30 min at 30℃. Simultaneously, the

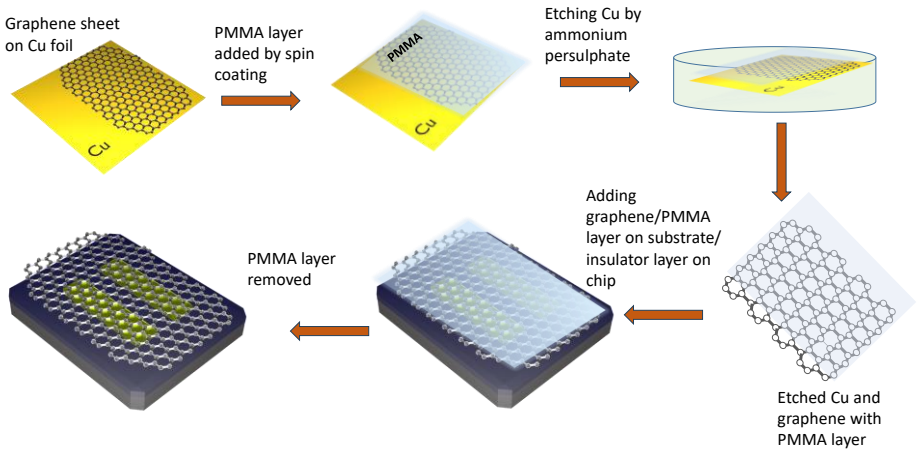

Figure 2.3: Schematic of graphene transfer.

substrate is taken out from the vacuum chamber and cleaned with isopropyl alcohol for 15 min. Next, the substrate with metal contacts is gently scooped through to make it stick to the PMMA/Gr film. The substrate is then kept in the air first for 4 hours and in vacuum for 5-6 hours.

2.1.5 Etching PMMA and Patterning Graphene Channel

The chips now should have graphene with PMMA on top of GaAs/Si_3N_4 and Si/SiO_2 substrates. To remove the PMMA on the graphene layer, each chip is first heated on a hot plate at 85℃ for 5 min and to make strong adhesion between graphene and the dielectric layer of the chips are heated for 25 min at 130℃. In the next step, the chip was taken out of the hot plate and submerged in an acetone solution. It was then heated at 60 ℃ for 1 hour and then the samples were transferred in IPA for 30 minutes at room temperature. The chips were then air dried and at this step the PMMA layer was removed. In order to pattern graphene channels in different devices, a positive photoresist S1813 was deposited, and spin coated under 2500 rpm. After spin coating the chip was baked at 100 ℃ for 1 min. A Mask Aligner MA6 was used to pattern the graphene channel. The exposure time with the UV lamp was 11 sec and after that the chip was dipped in a developer solution using MIF 319 for 30 sec. The chip was cleaned by dipping in DI water for 5 sec and then dried with nitrogen gas. After these steps, the chip was etched with oxygen plasma using Samco RIE-10NR for 45 second. Lastly, the chip was dipped in acetone followed by IPA for a minute and then dried using nitrogen gas. Figure 2.4 shows the patterning of graphene by photolithography and the final look of the patterned chip is shown in Figure 2.5.

2.1.6 Growing Protective Layer and Opening the Channel

To protect the chip from the ambient environment, a protective layer was grown on top of the Si chip with tantalum pentoxides (Ta_2O_5). A 5 nm Ta_2O_5 layer was grown using atomic layer deposition (ALD). During the Ta_2O_5 deposition the whole chip was covered by the protective layer but to do the electrical characterization the metal contacts need to be reopened. Therefore, we used photolithography to etch the Ta_2O_5 layer to reopen the back-gate, source, and drain contacts. A similar process was applied for this step. The final look of the GFET is shown in figure 2.5

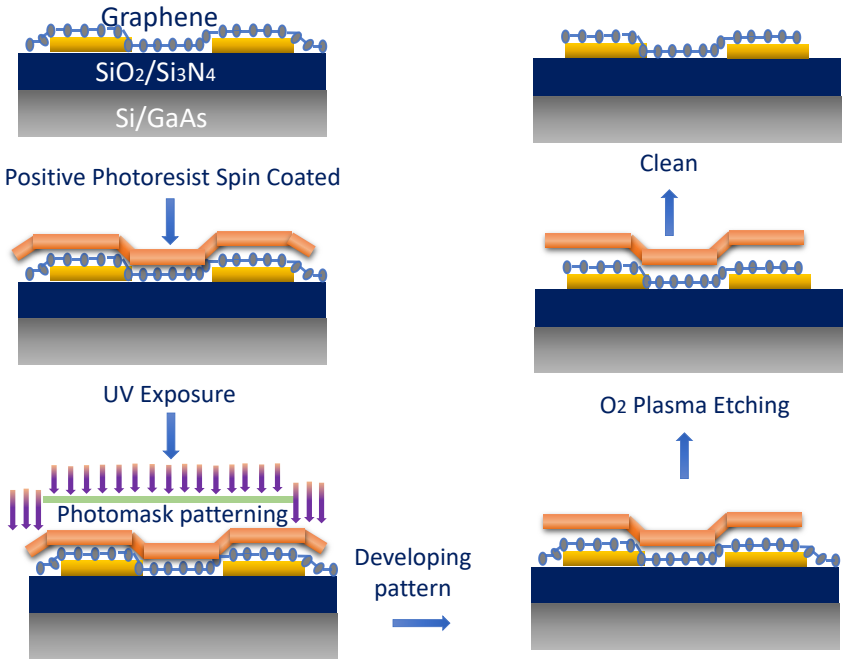

Figure 2.4: Schematic diagram of patterning graphene channel.

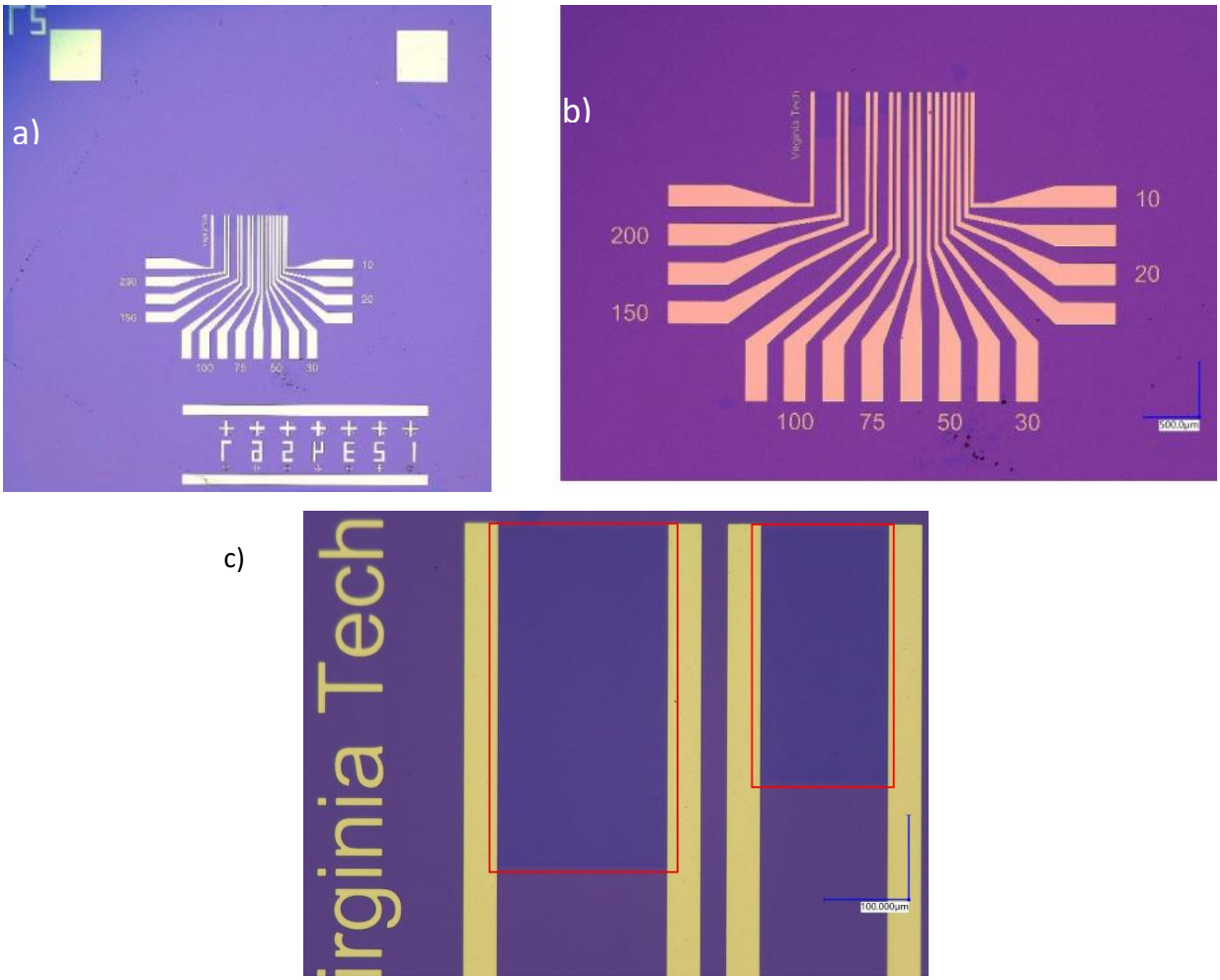

Figure 2.5: Final look of GFET photodetectors. Each 1 x 1 cm^2 chip contains a total 8 devices with different lengths, L, and widths, W, and each device under one chip are marked from D10 to D200. The LxW was designed such that the length is twice than the width. For example, the D10 has an area of 10 µm x 20 µm (a) Image of GFET chip with backgate and source -drain. (b) Image shows graphene channel fabricated between source and drain pair for each device. (c) Enlarged graphene channel between D150 and D200 devices.

2.2 Performance Characterization of GFET Photodetectors

The characterization of GFET photodetectors involves two major parts electronic and optical setups. Different electronic instruments were used in this experiment to measure the photoresponsity, time response and noise of the device. In this section, details of the setup are described with the specific type of measurements.

2.2.1 Optical Setup for GFET Characterization

Power Calibration for 532 nm Laser

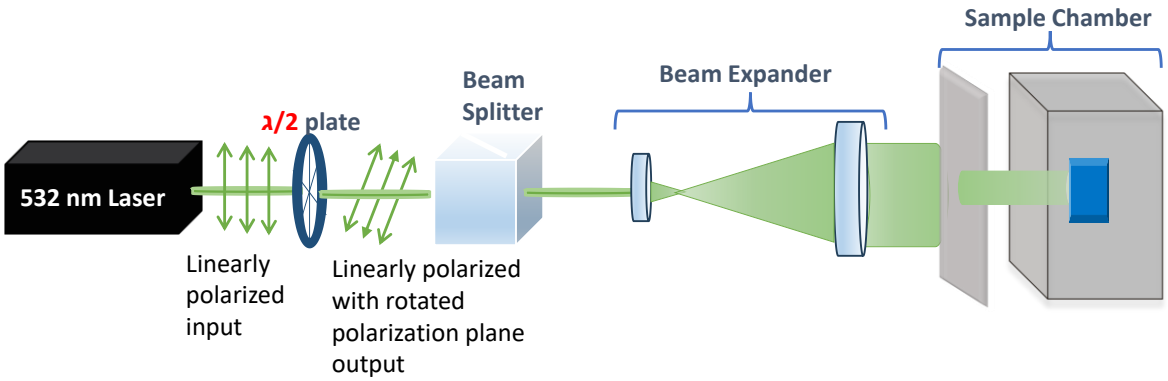

Figure 2.6: Optical Setup for 532nm Laser with a half wave plate, beam splitter, beam expander sample chamber, and sample.

For the optical characterization two different light sources – a 532 nm laser and a tungsten halogen broadband lamp - are used. To control the power from a laser a half wave plate and a beam splitter were used along with a beam expander to increase the beam size (Figure 2.6). The beam expansion was achieved through a configuration involving two lenses with focal lengths $f_1 = 25\ mm$ and $f_2 = 500\ mm$. Then a couple of optical mirrors were used to align the expanded and uniform beam onto the sample under examination. The sample chamber was made with black anodized aluminum to block any light from ambient and was designed to have a 10 mm diameter aperture at the center to pass the light through and shine on the sample. The power on device after using polarizer and beam splitter was calibrated using a Thorlabs S120VC - Standard Photodiode Power Sensor and 2.75mm pinhole. The recorded power corresponding to the half wave plate angle was fitted with

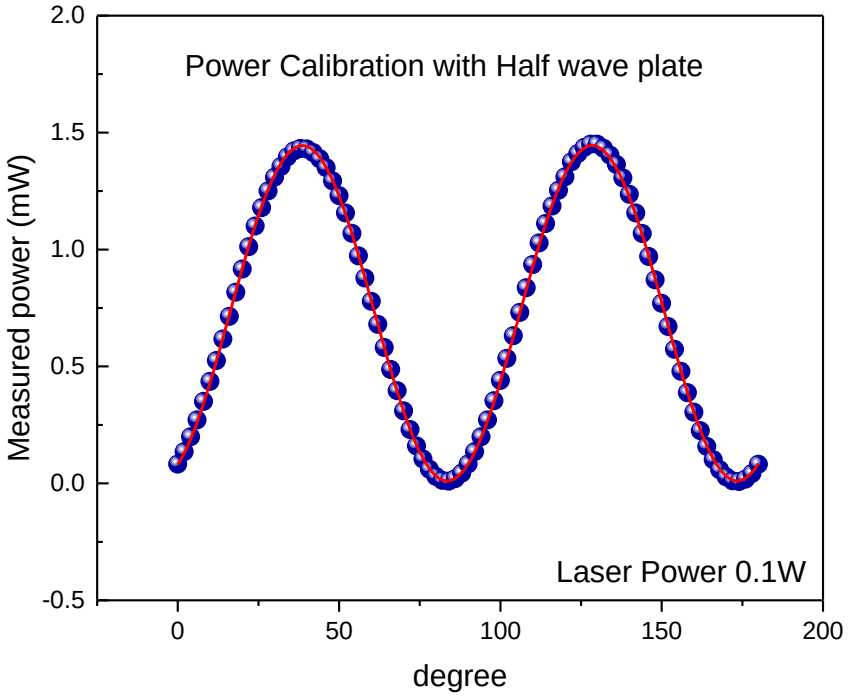

Figure 2.7: Power calibration for 532 nm laser setup with half wave plate and beam splitter.

sine square function (Figure 2.7). The parameters from the fitting were then used to calculate the exact angle required for each power and the power was divided by the area of the pinhole to get the power density (W/m^2). Finally, the power density was multiplied with the area of the device to get a power value on the device.

Power Calibration for Broadband Lamp

To get the device responsivity with different wavelengths a broadband lamp (BPS101 - B&W Tek) emitting light across a spectral range spanning from 350 nm to 2600 nm was also utilized. The performance was enhanced further through optimization using a beam expander. After optimization, Edmund bandpass filters were employed to choose particular wavelengths from the wide spectrum emitted by the broadband lamp. The power of the incident light from both the incoherent lamp and laser was further adjusted using neutral density filters, absorptive filters, and reflective filters obtained from Thorlabs and Edmund. Then the power on device for the lamp was measured using a silicon detector (200 nm – 1.1 μm) and a thermal detector (0.2 μm – 10.6 μm) from Thorlabs with a 2.75 mm pinhole and keeping the detectors at the sample spot. The power

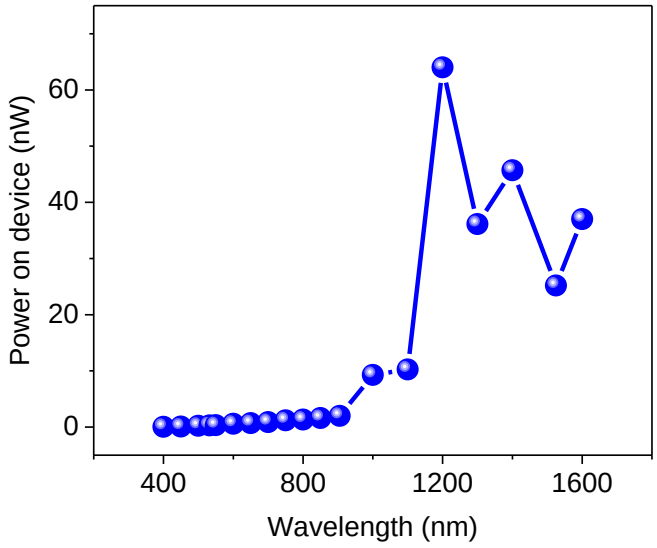

Figure 2.8: Power calibration for broadband lamp with D20 (LxW = 20 µm x 40 µm).

density through the pinhole was calculated with 2.75 mm pinhole area and calibrated for specific device area in the graphene FET chips. The power calibration for D20 with broadband lamp is shown in figure 2.8.

2.2.2 I-V measurement

The most basic measurement of our GFET photodetectors is observing the current due to applied voltage (I-V) curve. The I-V curve was measured using a two-point probe method with two Keithley source meters as the power supply. Keithley 2400 was used to supply a back gate voltage and Keithley 2450 was used for the source and drain (Figure 2.9). The device under test was scanned for back gate voltage from -30 V to +30 V and a fixed source to drain voltage (V_{DS}) of 0.2 V. The I-V curve showed the shift of Dirac point with and without illumination (dark) of light. After that the photocurrent was found by subtracting the dark signal from those with light using I-V curves.

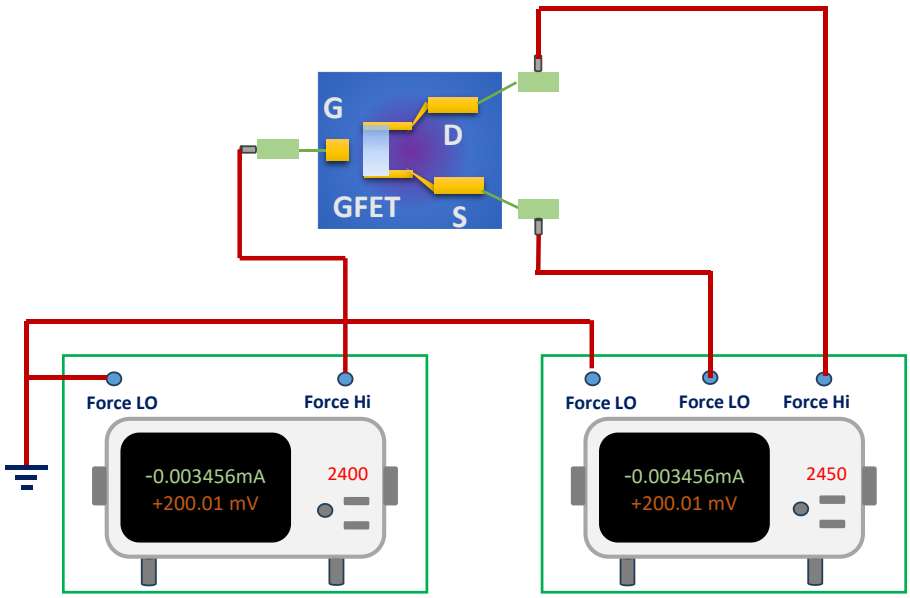

Figure 2.9: Two- wire electronic setup for I-V measurement.

2.2.3 Lock-in measurements

To characterize the GFET and find its responsivity, incident light was gradually reduced to very low powers. At very low power the signal is usually mixed with noises. To get the signal from noise a lock-in amplifier was used (Figure 2.10). Two source meter Keithley 2400 and 2450 was connected to the back gate and source of GFET respectively. The signal from drain was connected to a low noise current amplifier FEMTO DLPCA-200 and the output from the amplifier was connected to SR830 lock-in amplifier. The continuous light source was chopped at 10Hz frequency using a chopper. The chopper frequency was controlled by a frequency generator. As lock-in utilizes heterodyne principle to mix the input signal from source with a reference, the same chopper frequency was provided to lock-in. The back gate was then scanned from -30V to +30V and the photocurrent curve was generated.

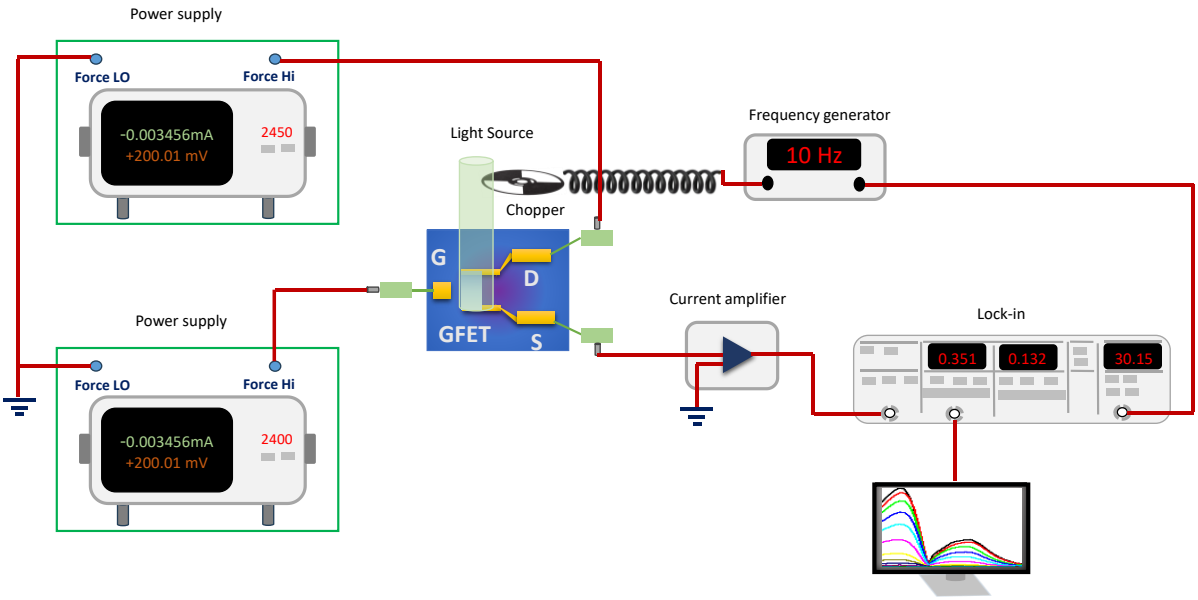

Figure 2.10: Schematic of setup for lock in measurement with two-point probe system.

2.2.4 Time Response Measurement

For the time response characterization of GFET devices the rise time and recovery time was measured using the setup as shown in Figure 2.11. The setup involved two source meter, an acousto-optic modulator, a low noise amplifier (FEMTO DLPCA-200) and a mixed signal oscilloscope (Tektronix MSO2000B/DPO2000B). The acousto-optic modulator (AOMO 3200-121) was used to chop the light into an on/off pulse at a specific frequency. The frequency provided to the (AOM) by the signal generator was far higher compared to any mechanical chopper or shutter. For the response measurement, first the back gate voltage corresponding to the maximum photocurrent was determined using the lock in setup. Then, for a fixed back gate and source-drain voltage the device response curve was obtained from the oscilloscope as a function of voltage and time. The curve was then fitted using an exponential function and from the fitting the rising and recovery time was obtained.

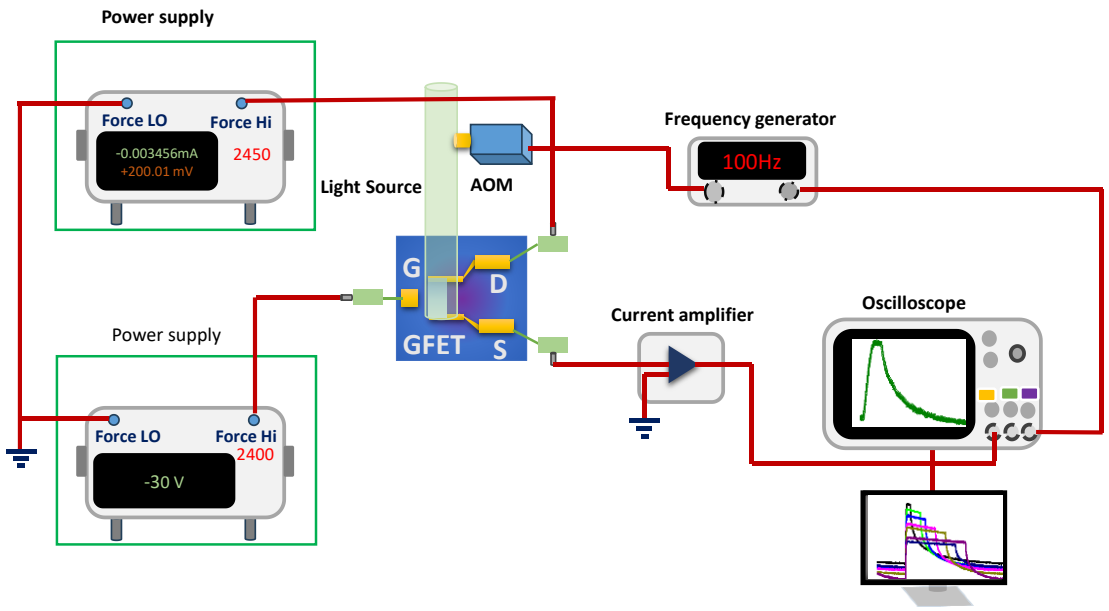

Figure 2.11: Electronic setup for time response measurement.

Power Calibration for AOM Chopper

The power calibration for AOM depended on several parameters such as applied laser power, half wave plate angle, width (ON) and delay (OFF) ratio of the given pulse and total pulse duration (frequency). First, the calibration was done for the half wave plate angle and a fixed laser power and pulse duration. The angle at which the power is maximum is chosen and the ratio of ON/(ON+OFF) pulse duration was changed as shown in figure 2.13. The change with ON time over the total pulse duration shows a linear increase in power for different applied laser power. The power measured with a 2.75mm pinhole was then used to get the power density and power on device.

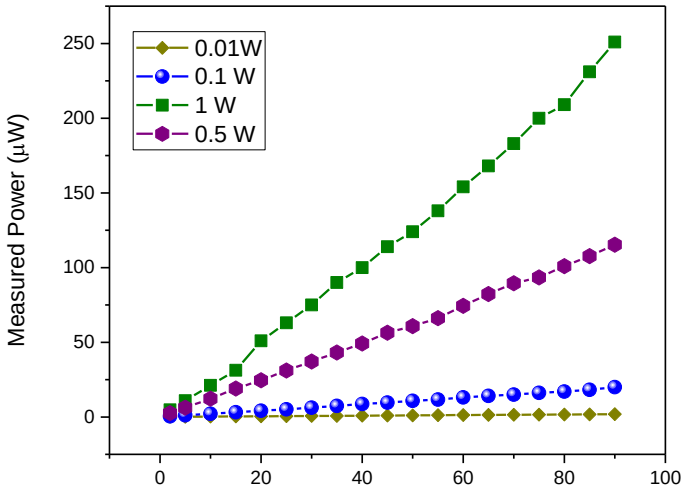

Figure 2.12: Power calibration for AOM.

2.2.5 Noise Level Measurement

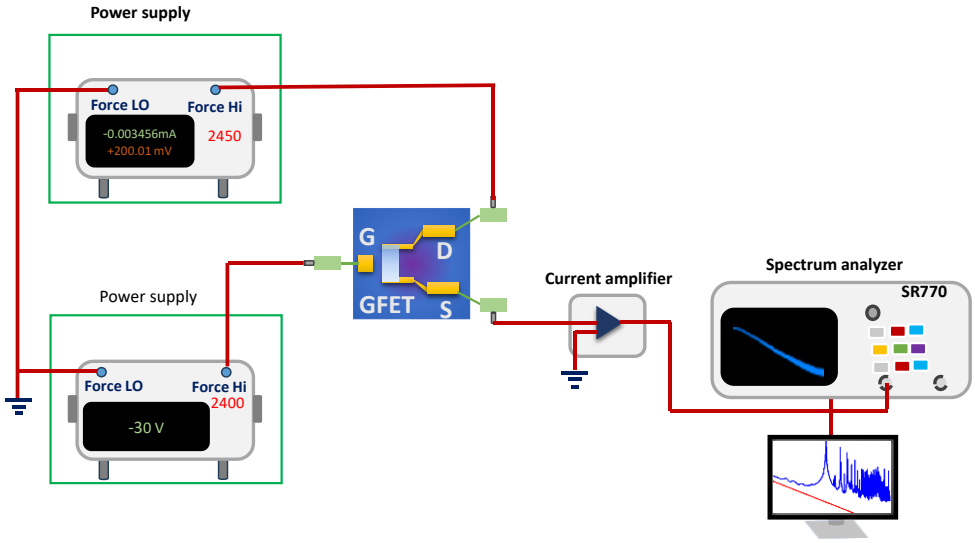

Figure 2.13: Schematic of electronic setup for noise level measurement.

The noise level of the GFET detectors was assessed using the setup depicted in Figure 2.14. Similar to the configurations used for I-V and lock-in measurements, the back gate and source-drain voltage were supplied by two source meters, the Keithley 2400 and 2450. The drain was connected to a low noise amplifier, and the amplifier's output was linked to the spectrum analyzer (Stanford Research 770 – SR770). The SR 770 has a high dynamic range (90 dB) and a frequency range of 100 kHz. The measurement parameters included averaging over 1500-3000 points using root mean square (RMS), averaging in linear mode, DC coupling, ground electrical connection, measurement of power spectral density in dBV/dBEU, and uniform sampling window.

Chapter 3

Result and Discussion

In this section, the mobility, responsivity, and time response performance of GFET photodetector on p-doped Si and GaAs substrates will be discussed. In addition to the performance of the photodetectors a highlight of differences between them will be provided.

3.1 Band Bending at GFET under Dark Condition

The fabrication of GFET detectors consists of a thick semiconductor substrates, insulating layer and a single layer of graphene acting as the active channel. The work function for *p*-doped GaAs, *p*-doped Si and graphene are 5.032 eV [98], 5.07 eV [128] and 4.56 eV [129], respectively. This difference in work function of substrates and graphene causes a downward band bending for the semiconductor-substrate/insulating layers (GaAs/Si_3N_4 and Si/SiO_2), which have a contact with graphene. The band bending between the contacts is much like metal/insulator/semiconductor (MIS) forming a potential well at the substrate/insulator interface, trapping electrons near the interface and inducing holes in graphene channel by capacitive coupling. The induction of holes causes the fermi level of graphene to shift from E_{F0} to E_{F1} causing a downward band bending (Figure 3.1 a). As the carriers in graphene has high mobility and electrons are trapped at the interface, a bias voltage applied between source to drain will cause holes to move in the channel, generating current. Similarly, for *n*-type substrate the charge carrier trapped in the substrate/insulator interface are holes and electrons are induced in graphene channel causing an upward band bending. Along with the type of interface between insulator and *p*-type or *n*-type substrate the current generation also depends on the back gate voltage. When a negative voltage is applied at the back gate more electrons are pushed toward the interface and since the insulating surface must stay neutral more holes are induced in graphene. As a result, more holes will circulate in the graphene channel, and we will observe high current. If we keep increasing the back gate voltage in the positive direction the number of trapped charge carrier changes and we observe a reduced current. At a certain voltage the number of holes and electrons in graphene is equal and we observe the lowest current. This point is called the Dirac or charge neutrality point.

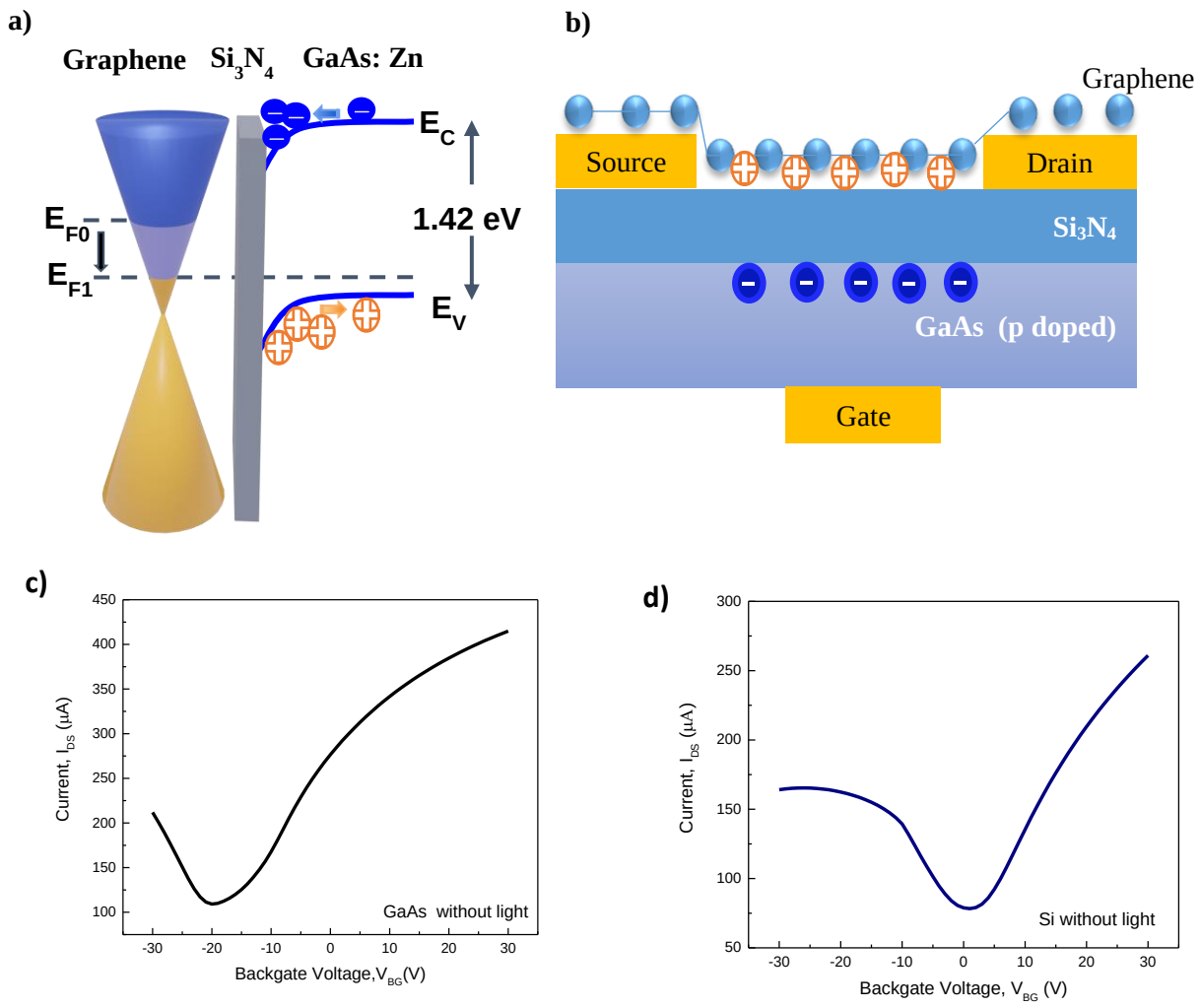

Figure 3.1: Illustration of band bending in GFET photodetectors for p-doped GaAs substrate (a) Band diagram for heterojunction in Gr/Si_3N_4/ GaAs: Zn and fermi level shift in graphene due to the accumulation of charged carriers at the GaAs: Zn/ Si_3N_4 interface. (b) Schematic of GFET photodetector on GaAs: Zn substrate, graphene (blue), source and drain contacts (yellow), and Si_3N_4/ GaAs: Zn layer. The blue and orange circles represent electrons and holes respectively. (c) The current-voltage curve of a GFET photodetector on the GaAs: Zn substrate without Ta_2O_5 protective layer and applied V_{DS}= 0.2 V under dark. (d) The current-voltage curve of a GFET photodetector on the Si:B substrate with Ta_2O_5 protective layer and applied V_{DS}= 0.2 V under dark condition.

For an ideal pristine graphene, the Dirac point should be observed exactly at zero voltage but as the graphene is contacting with the insulator/substrate and the Dirac point shifts away from zero. The current response across the graphene channel is plotted against the back gate voltage and shown in Figure 3.1 c and d.

3.2 Mobility for Charge Carriers in Graphene Channel

A free-standing graphene with carriers is reported to have very high carrier mobility of 200, 000 $cm^2V^{-1}s^{-1}$ [21]. The high mobility of carriers in graphene is greatly reduced to about 2000-25,000 $cm^2V^{-1}s^{-1}$ [19, 101-103] when placed on SiO_2 layer or substrates. The wide variation of carrier mobility in graphene originates from several factors such as defects in substrates [104], residuals from fabrication [25], charge impurity and interfacial phonon scattering [104,105]. The inhomogeneity of charge impurity and its scattering is one of the main reasons for GFETs to have low mobility in graphene [106-110]. The origin of the scattering induced by the charge impurity in GFET can be explained in terms of long-range coulomb scattering [84]. The long-range coulomb scattering is reported to be minimized using the screening effect of high dielectric constant (κ) material on graphene. A dielectric material with $\kappa = 20 – 50$ has been reported to preserve mobility in GFET [83,84,111,112]. Moreover, the addition of dielectric layer on graphene also protects the device from environmental exposure to contaminants. From several available choices for high-κ materials, tantalum pentoxide (Ta_2O_5) stands out as a promising material owing to its high dielectric constant (22 - 60), minimum leakage current and other properties [113-119]. For our GFETs we have deposited a 5 nm Ta_2O_5 layer on graphene using atomic layer deposition (ALD) [120-123] on the GFET devices. For the thin atomic layer of Ta_2O_5 it has been reported that the layer does not take part in photo-generated carriers under light with wavelengths longer than 300 nm [46,80]. However, for GaAs, no Ta_2O_5 layer was deposited, as we wanted to observe the performance of only p-doped GaAs without any capping layer. To extract carrier mobility of graphene-based device three different techniques are available [124], including the Drude model, constant mobility model [125] and Hall mobility [105].

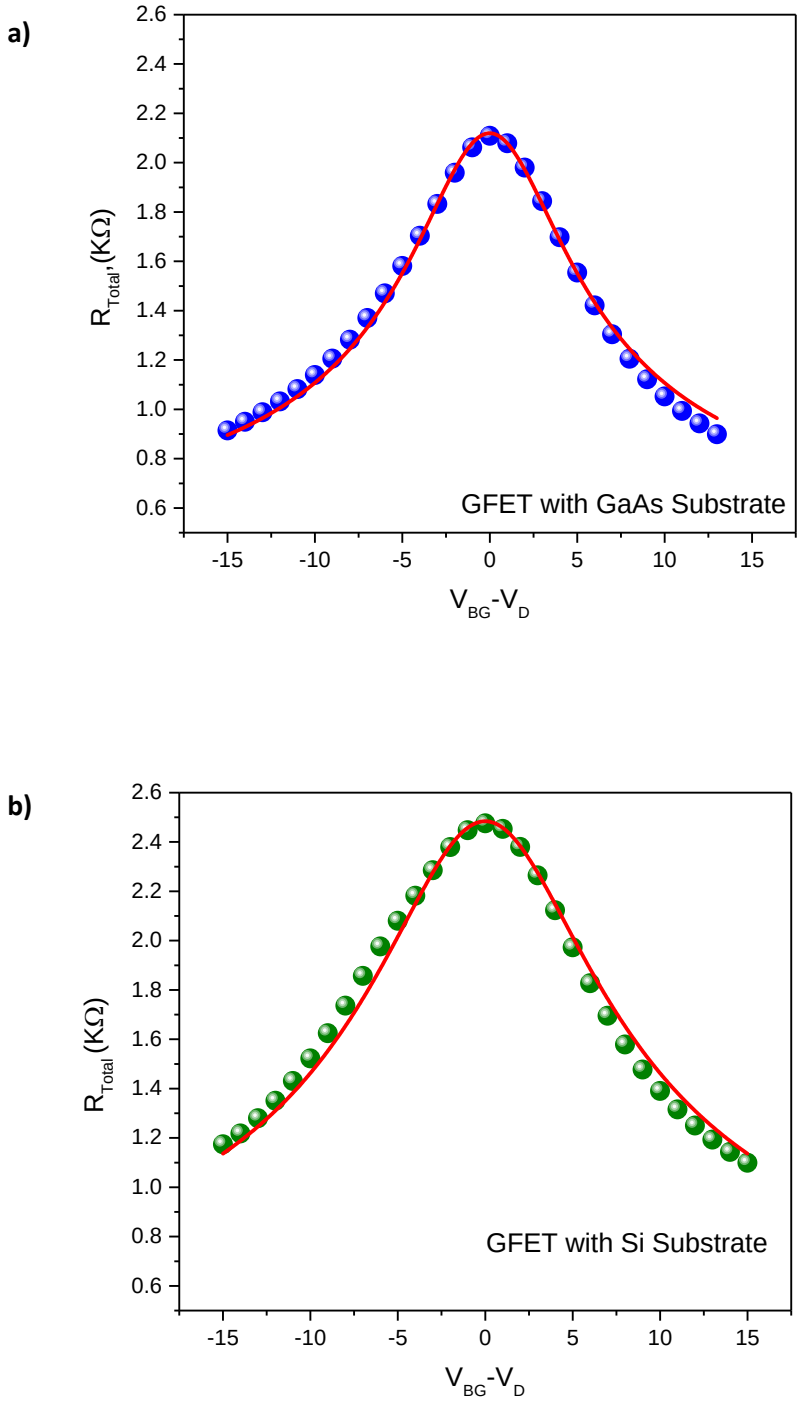

Figure 3.2: Resistance vs voltage characteristic curve for GFET with p-doped (a) GaAs and (b) Si substrate for device area 50 µm x 100 µm (D50) under $V_{DS} = 0.2V$ and dark condition. The red line is fitted using equation 3.1 and gives the mobility value.

For constant mobility model, the mobility was found from the fitting of the relationship between resistance and back-gate voltage curve, given by,

$$R_{Total} = 2R_c + R_G = 2R_C + \frac{{}^{L}/_{W}}{e\mu\sqrt{{\eta_0}^2 + (\frac{C_g}{e}(V_{BG} - V_{Dirac}))^2}} \quad , \qquad (3.1)$$

where R_{Total} is the total resistance, R_c is the contact resistance, R_G is the resistance of the graphene channel which can have different length, L, and width, W, between source and drain, e is the charge of electron, η_0 is the carrier concentration induced by charge impurity at the graphene/dielectric interface, $\eta_g = \frac{C_g}{e}(V_{BG} - V_{Dirac})$ is the carrier concentration due to back-gate voltage away from Dirac point voltage, V_{Dirac} and the gate capacitance, $C_G = \frac{\varepsilon\varepsilon_o}{d} = \sim 22.14$ nF/cm^2 for GaAs substrate with Si_3N_4 dielectric layer with a thickness, d = 300 nm, and $C_G = \sim 11.51$ nF/cm^2 for Si substrate with SiO_2 dielectric layer with a thickness, d = 300 nm. The fitted red curves using the equation (3.1) give the carrier mobility for graphene on Si_3N_4 (Figure 3.2 a) of ~7053 $cm^2V^{-1}s^{-1}$ and for graphene on SiO_2 (Figure 3.4 b) of ~5677 $cm^2V^{-1}s^{-1}$. The high carrier mobility of both devices is found to be in the same order, which confirms good adhesion of graphene with the dielectric layer and good connection of the protective layer (Ta_2O_5) on graphene for the Si device. One thing we observed here is that even though GaAs has wider bandgap and higher carrier mobility compared to Si material, the insulating layer plays a much more important role for mobility.

3.3 Introduction to the Photogating Effect in GFET

The working principle of GFET based on photogating effect is briefly described in section 1.3.3 and illustrated in figure 3.3. Figure 3.3 shows the photogating effect in p-doped GaAs substrate with Si_3N_4 insulating layer under light illumination. When incident photon has higher energy than the bandgap of the substrate material electron hole pairs are generated (photo-generated carriers). Figure 3.3 a shows the photo-generated carriers are separated due to potential at the interface and electrons are trapped at the interface (*p*-doped substrate/insulator). Extra carriers populated at the interface widen the depletion region. As a result, additional holes are induced in the graphene channel and a photocurrent will be generated when a bias voltage is applied between source and

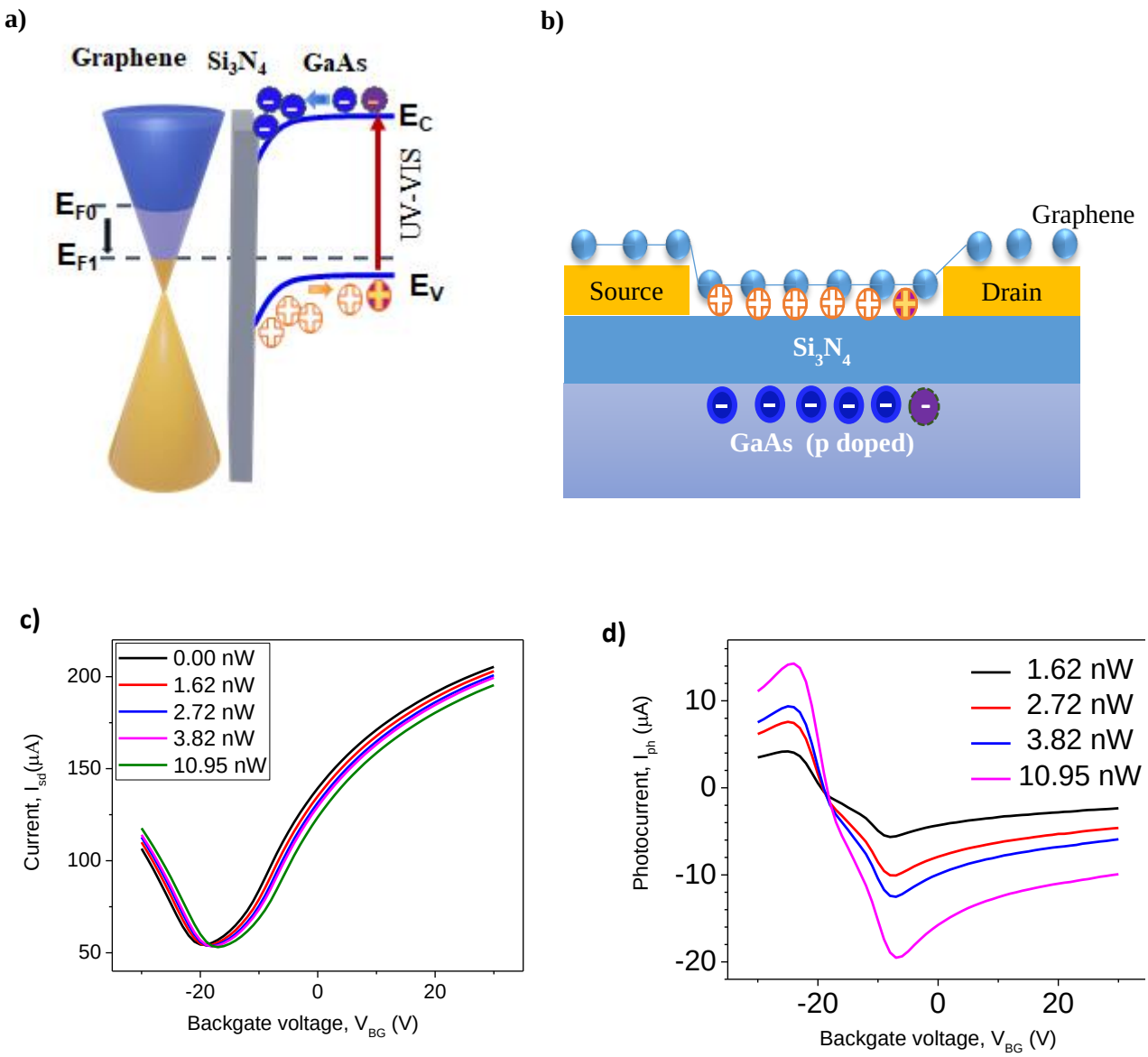

Figure 3.3: Illustration of photogating effect in GFET photodetectors for p-doped GaAs substrate (a) Band diagram for heterojunction in Gr/Si_3N_4/ GaAs: Zn and accumulation of photogenerated charged carriers at the GaAs: Zn/ Si_3N_4 interface. (b) Schematic of GFET photodetector on GaAs: Zn substrate, graphene (blue), source and drain contacts (yellow), and Si_3N_4/ GaAs: Zn layer. The purple and orange circles represent photogenerated electrons and holes respectively. (c) The current-voltage curve of a GFET photodetector on the GaAs: Zn substrate without Ta_2O_5 protective layer and applied V_{DS}= 0.2 V under light illumination (d) The photocurrent curve of a GFET photodetector on the GaAs substrate.

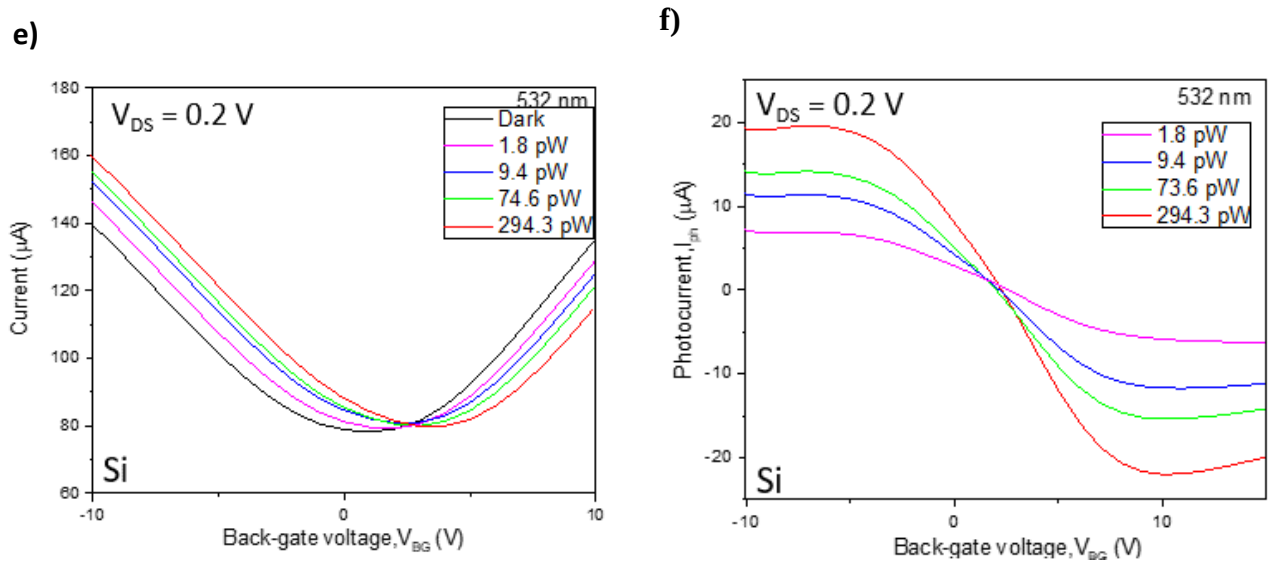

Figure 3.3: (e) The current-voltage curve of a GFET photodetector on the Si:B substrate with Ta_2O_5 protective layer and applied V_{DS}= 0.2 V under light illumination (d) The photocurrent curve of a GFET photodetector on the Si substrate.

drain contacts (Figure 3.3 b). Electrical currents of the GFET observed under dark conditions and with light illumination shown in Figure 3.3. A shift of the transfer curves to the positive voltage with increasing light power has been observed. As a result, the Dirac point shift rightward for *p*-type material.

A similar observation has been reported for the GFET on p-Si substrate (Figure 3.3 e, f) The I-V curves with and without light for graphene on *p*-Si devices are shown in Figure 3.3 e. A shift rightward of the Dirac points in both device structures indicates the p-doped graphene channel on these photodetectors. The photocurrent in Figure 3.3 d, f shows an increase with increasing power. An increasing of the photocurrent with power shows an increase in the number of charge carriers participating in the photogating effect.

3.4 Photocurrent Characteristics with Increasing Source- Drain Voltage

The photocurrent behavior with increasing source-drain current, V_{DS}, was also characterized from 0.05 to 0.75 V. Figure 3.4 shows I-V characteristics curves for device area 50 µm x100 µm (D50)

as V_{DS} increases. The I-V curve with increasing V_{DS} shows an increase in current. As explained in section 3.3 under light conditions, a change of the current has been observed.

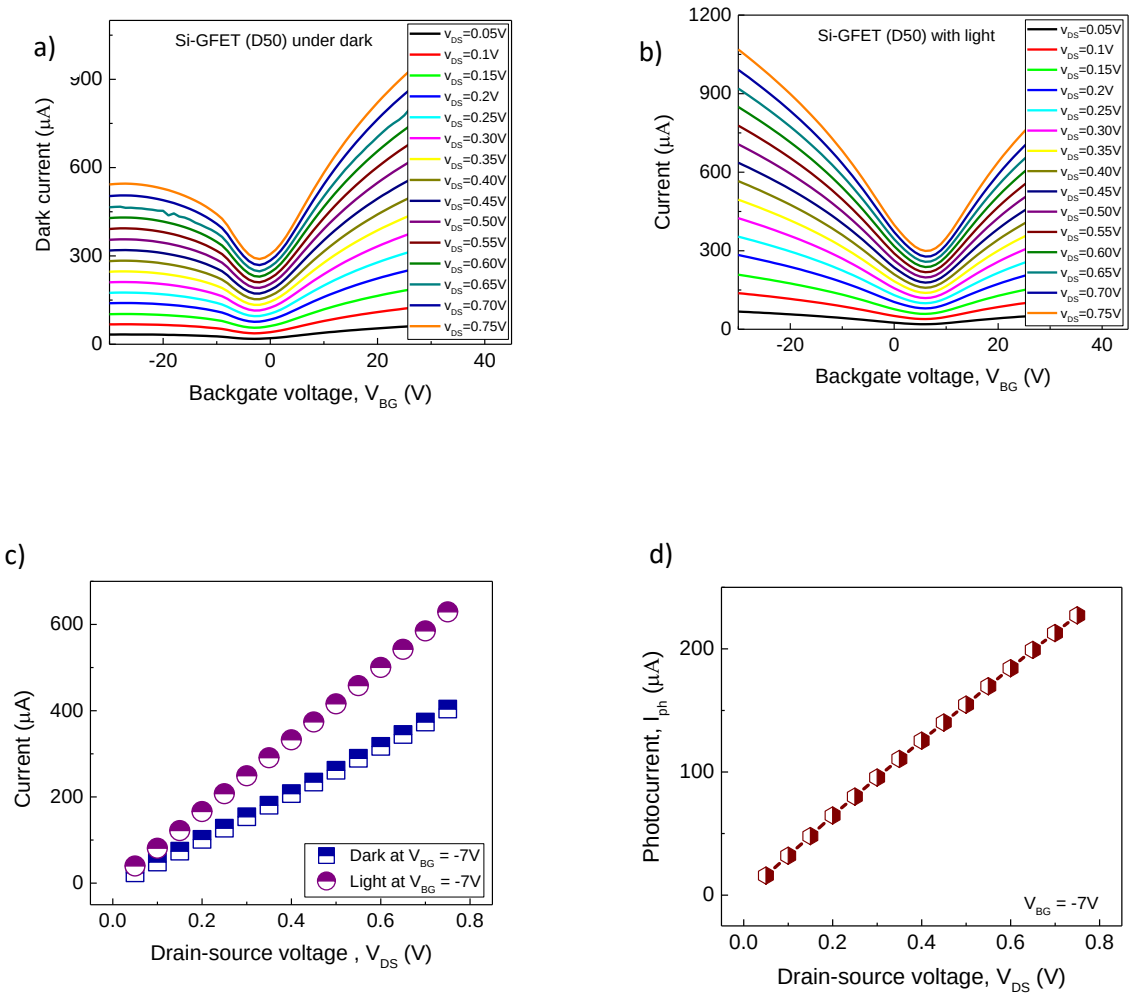

Figure 3.4: I-V characteristics curve for Si D50 = (50 µm x 100 µm) a) without light b) with light condition with V_{DS} = 0.05V to 0.75V. (c) Current at V_{BG} = -7V under dark and with 532 nm light condition. (d) Photocurrent with change of source-drain, V_{DS} voltage from 0.05V to 0.75V with 532 nm laser at fixed back gate V_{BG} = -7V for Si– GFET.

The change can be seen here also when the source and drain voltage, V_{DS}, increases. As V_{DS} changes, the electric field across the channel enhances which in turn increases the velocity of charge carriers (related to the mobility) allowing more current to flow from drain to source. By

determining the photocurrent, $I_{ph} = I_{light} - I_{dark}$, where I_{light} and I_{dark} are the currents under the illumination and dark conditions, respectively, photocurrent increases in response to the source-drain voltage (Figure 3.4 b). A linear function has been observed for the GFET on *p*-Si substrate.

3.5 Photo responsivity of GFET on p-doped GaAs and Si Substrate

3.5.1 Responsivity of GFET on *p*-doped GaAs

To understand the effect of light on p-doped GaAs substrate, GFETs have been characterized systematically with different power from visible to near IR light. The measurements were all done at room temperature with different back-gate voltage and a fixed source-drain, V_{DS}= 0.2V.

The I-V characteristic curve under light was measured using lock-in setup (Figure 3.5 a). For lock in measurement the light was chopped at 10Hz. The same chopping frequency was also used as the reference for lock in. The back gate voltage was changed from -30 V to +30 V and under a 700 nm wavelength excitation. The light power was changed from 350 PW to 0.3 PW.

The maximum photocurrent was observed to be at V_{BG}=-26V (Figure 3.5 a) and recorded directly as the photocurrent (Figure 3.6 b) under 10 Hertz. The photo responsivity, R_{ph} was calculated from, $R_{ph} = {I_{ph}}/{power\ on\ device}$ and shown in Figure 3.5 c. At low power region from 0.3 PW to 17.5 PW, the photocurrent response shows a linear dependence. The photon absorption at such low power generates well separated electron–hole pairs. The higher the number of electrons or holes the more it contributes to current. As a result, linear behavior is observed under low power. The responsivity calculated at low light power shows a constant, which has a maximum of about ~3.6×10^5 A/W at 0.3 pW.

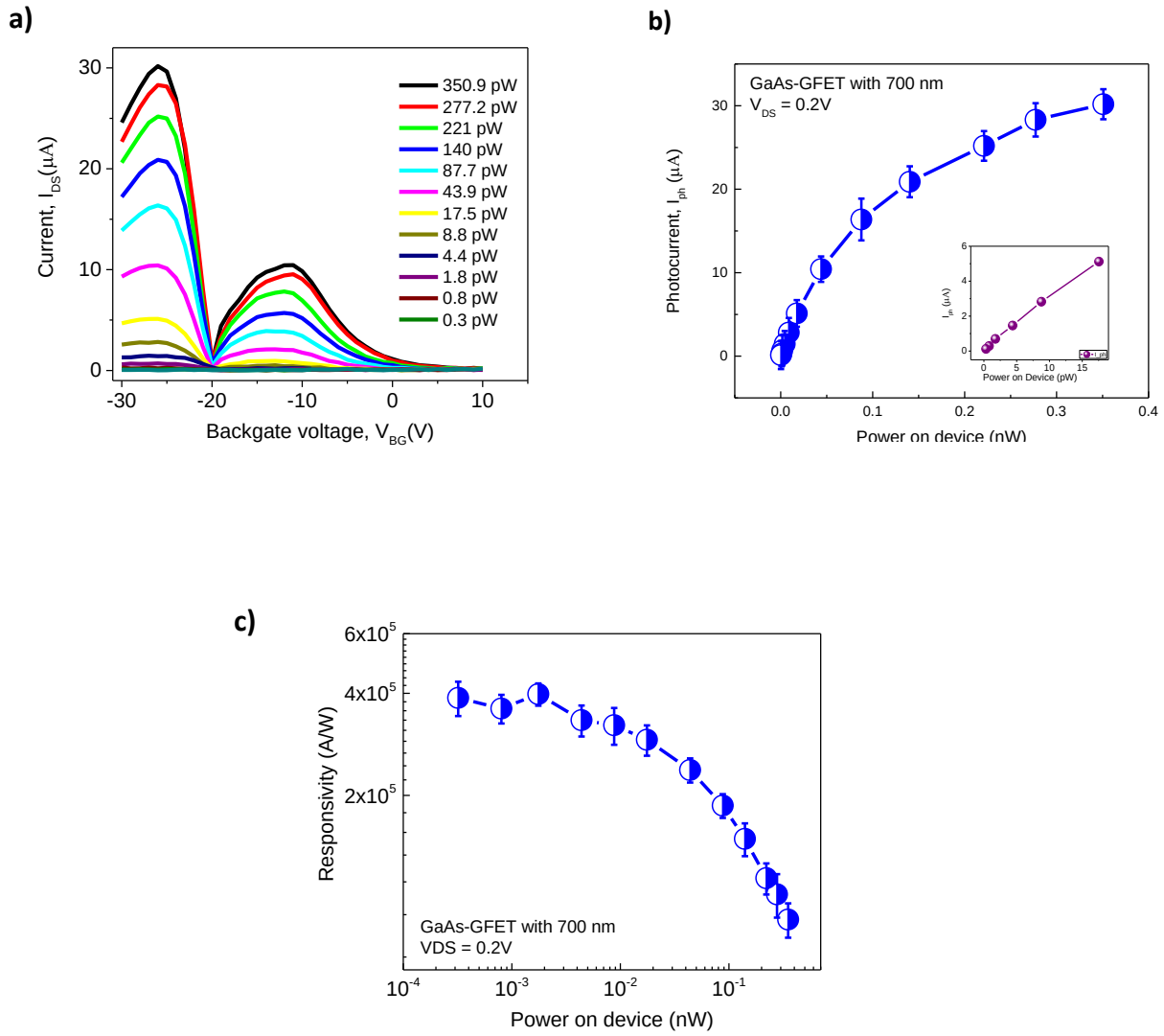

Figure 3.5: GFET response to light illumination on p-doped GaAs substrate at $\lambda = 700$ nm and $V_{DS} = 0.2V$ (a) I-V characteristic curve of GFET at different light powers using lock in measurement. (b) Photocurrent measurement at back gate voltage, V_{BG} = -26V with different light power from I-V. (c) The responsivity of GFET characterized using ratio of photocurrent and device area under 700 nm light illumination.

However, at high power region, the absorption causes to generate more electron-hole pairs and some of the holes recombines with the electron. Also, a number of recombination paths such as the radiative and non-radiative processes occur under a high-power excitation including Auger non-radiative recombination, defect and trapped states capturing photo generated carriers, reducing the number of electrons trapped at the *p*-semiconductor/insulator interface. Thus, the

number of additional holes in the graphene channel induced by the interface potential reduces, and the photocurrent grows slowly with increasing power. As a result, the responsivity at high power is lower.

3.5.2 Responsivity of GFET on *p*-doped Si

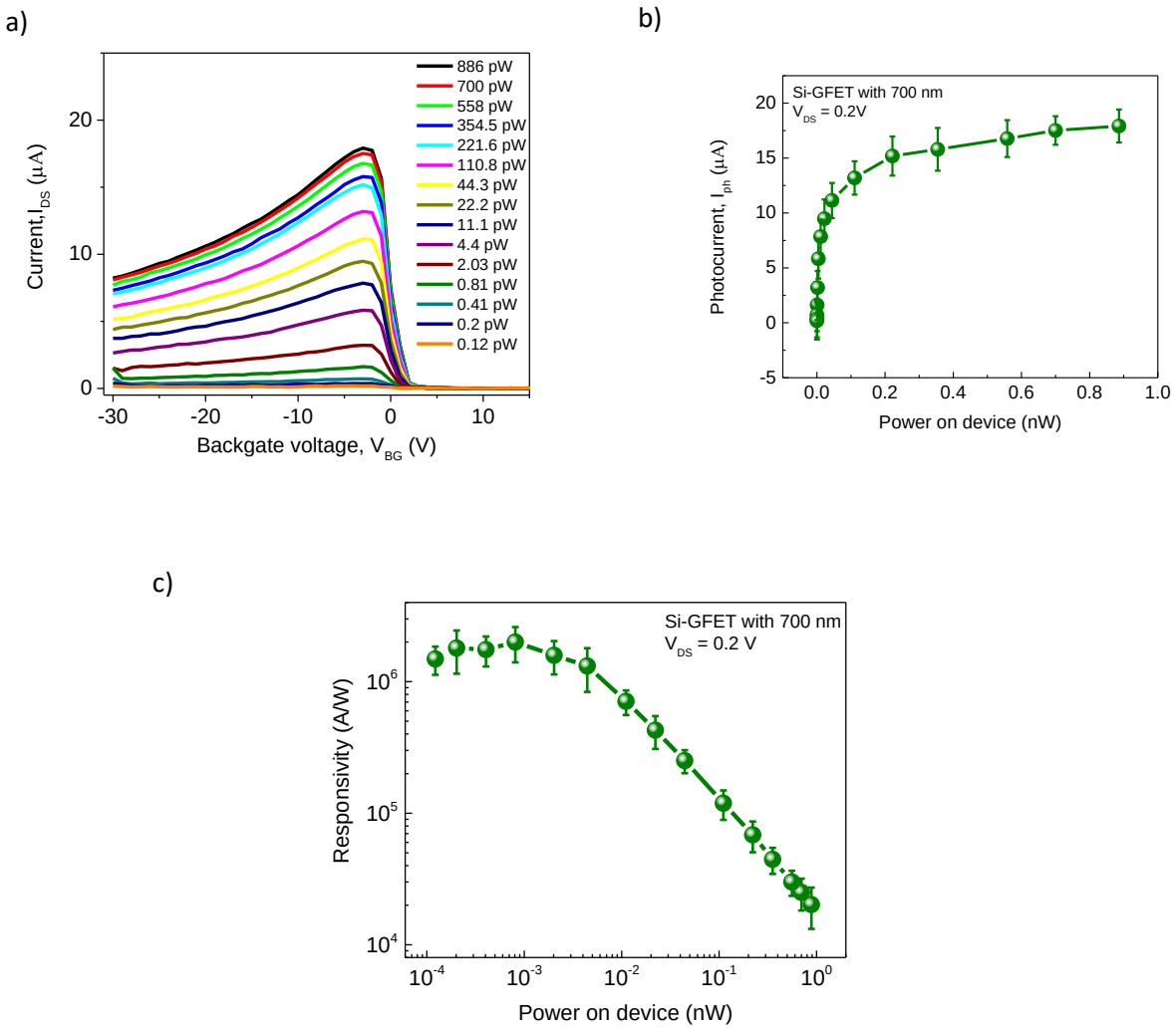

Figure 3.6: GFET response to light illumination on P-doped Si substrate at $\lambda = 700\ nm$ and $V_{DS} = 0.2\ V$ (a) I-V characteristic curve of GFET at different light powers using lock in measurement. (b) Photocurrent measurement at back gate voltage,V_{BG} = -3V with different light power from I-V curve. (c) The responsivity of GFET characterized using ratio of photocurrent and device area under 700 nm light illumination.

A similar observation for the photocurrent and photo responsivity of GFET with lightly doped Si with boron was also characterized. The GFET on Si was fabricated with a protective layer Ta_2O_5 and characterized for visible to near infra-red under the source-drain voltage of 0.2 V. The I-V curves of the device shift with light as GFET on GaAs substrate, in which the power varied from 886.6 PW to 0.12 PW under 700 nm light illumination (Figure 3.6). Both types of devices follow a similar behavior in the photo detection at low and high-power regions. The photo responsivity of device on silicon substrate is about ~1.75×10^6 A/W for 0.405 PW.

3.6 Wavelength Dependence of GaAs and Si based GFET

The responsivity at different wavelengths from 400 to 1600 nm was collected using a narrow bandpass filter with a broadband lamp (BPS101 - B&W Tek) and shown in Figure 3.7. For the GFET on GaAs substrates, responsivity was observed to be high at shorter wavelengths (400-800 nm) and highest at 700 nm with $V_{DS} = 0.2V$. Similarly, for the GFET on Si we observed a high responsivity of 10^6 A/W below bandgap wavelength till ~1000 nm. In order to compare, the two GFETs on GaAs without Ta_2O_5 and Si with Ta_2O_5 layer we used a factor of 10 which has been reported [46]. The high responsivity in the order of ~10^6 A/W above bandgap can be attributed to the band-to-band excitation in the substrate. Consequently, at the longer wavelengths and specifically under the excitation of photons with the energy below the bandgap of both GaAs and Si substrates, the responsivity sharply falls off from ~10^6 A/W to 26 A/W. As can be seen from Figure 3.7, a high photoresponsivity under the excitation with wavelengths longer than 875 nm and 1100 nm, corresponding to the bandgap energy of GaAs and Si materials, still has been observed. This could be ascribed to the fact that both the GaAs and Si substrate used in this study were lightly p-doped. The doping produces impurity states inside the bandgap of the semiconductor materials, related to Urbach tail states [126]. As a result, the high gain, bandgap of the GaAs and Si, and the doping concentration lead to the long wavelength detection in these photodetectors such as ~ 10^3 A/W for GaAs GFET devices at 1000 nm, and 26 A/W on Si substrate devices at 1525 nm.

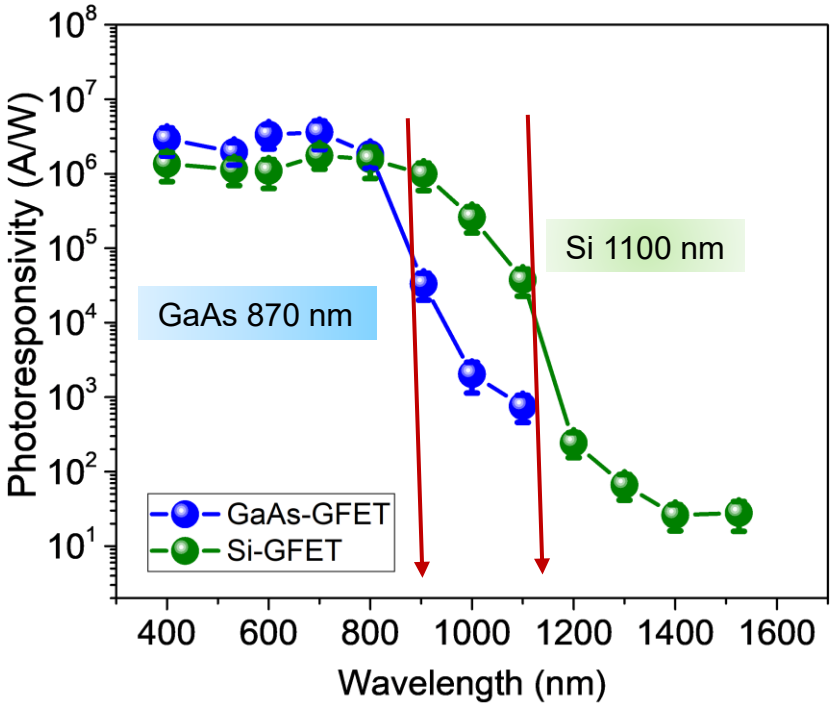

Figure 3.7: Responsivity comparison of GFET with different wavelength from 400nm to 1600nm for Si and GaAs substrate for device size 20$\mu m \times 40\mu m$.

3.7 NEP Results

One of the most important performance metrics for photodetectors is the sensitivity of the device to the application of light. To measure the sensitivity two quantities such as the noise equivalent power, NEP, and the specific detectivity, D* with units of W/$\sqrt{Hz}$ and cm.$\sqrt{Hz}$/W (Jones) respectively the following relations can be used,

$$NEP = \frac{Noise\ Current}{R_{ph}} = \frac{\sqrt{S_I(thermal)+S_I(Shot)+S_I(1/f)}}{R_{ph}} \text{ and,}$$

where $S_I(thermal)$, $S_I(Shot), S_I(^1/_f)$ are the spectral power density due to thermal noise, shot noise, and $1/f$ flicker noise respectively and R_{ph} is the photoresponsivity.

$$D^* = \frac{\sqrt{A_{channel}}}{NEP}$$

Where $A_{channel}$ is the active area of the transport channel in cm^2.

The details of each of these parameters have been discussed in sections 1.4.4 and 1.4.5.

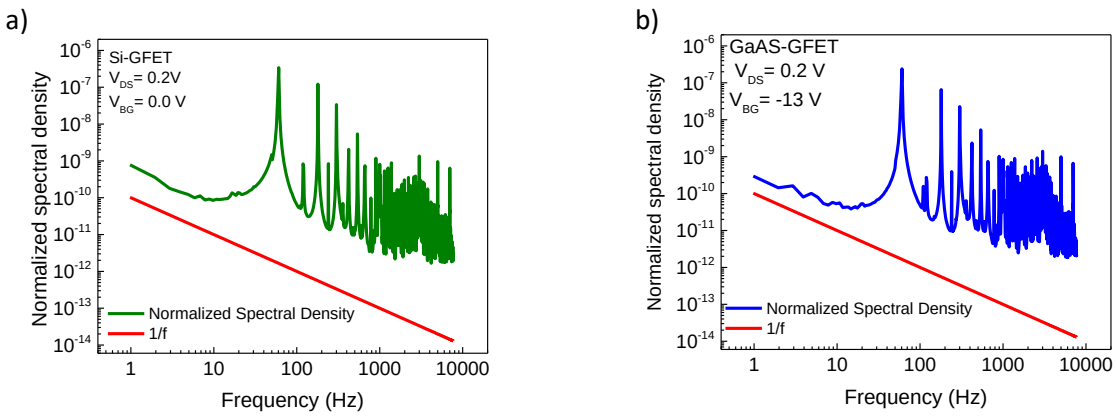

Figure 3.8: Normalized spectral density with frequency under dark condition. (a) Si-GFET device (b) GaAs-GFET device.

The normalized spectral density was obtained using a low noise amplifier (DLPCA 200) and a spectrum analyzer (SR 770) under dark conditions. The device used for the characterization had a length of 50 µm and width of 100 µm. The back-gate for Si-GFET and GaAs-GFET were fixed at 0 V and -13V respectively and source-drain voltage, V_{DS} = 0.2V. Figure 3.8 shows the normalized spectral density for both devices. They are quite similar. Furthermore, the NEP and D* characteristics are shown in figure 3.9. Both the NEP and D* values for the devices are of the same order, in which the GaAs-GFET seems a little better. The NEP and D* values observed for the devices show a wavelength dependence. The highest value for NEP observed was 10^{-15} W/$\sqrt{Hz}$ at and for D* it was 10^{12} Jones. The values collected from these devices are capable of detecting weak signals with low noise level.

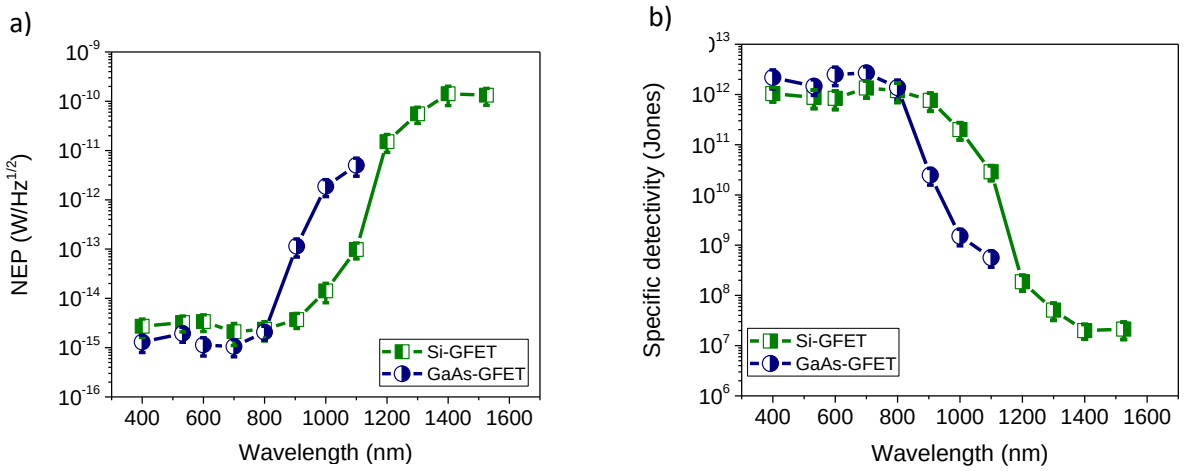

Figure 3.9: NEP and specific detectivity performance of both Si-GFET and GaAs-GFET under dark condition. (a) Comparison between the NEP values of Si-GFET and GaAs-GFET device (b) Comparison of specific detectivity of Si-GFET and GaAs-GFET device with V_{BG} = 0V for Si and V_{BG} = -13V for GaAs respectively.

3.8 Time Response Dynamics

The time response behavior of a photodetector is a key factor in determining the performance of the detector. It can quantify how fast the device responds to light. As all the performance metrics show a similar behavior for Si-GFET and GaAs-GFET for time dynamics, measurement we have focused on one substrate Si-GFET. We have characterized the Si- GFET with V_{DS} = 0.2 V and V_{BG} = - 2 V at room temperature and with 532 nm laser as the light source. The back-gate was chosen at -2 V as the photocurrent was maximum at that voltage [127]. An acousto-optic modulator (AOM) was used to chop the continuous 532 nm laser source into light pulse. In addition, an oscilloscope was used with the AOM to get the photocurrent response with time. The limitation of our experimental setup was that the AOM can obtain a rise time of 18 ns.

3.8.1 Time Response with Fixed Input Power

Before taking the rise and fall time measurement, understanding the effect of width/period or ON/(ON+OFF) is crucial. In Figure 3.10 shows how the time response varies as a function of pulse width when the total power coming from our optical setup is fixed.

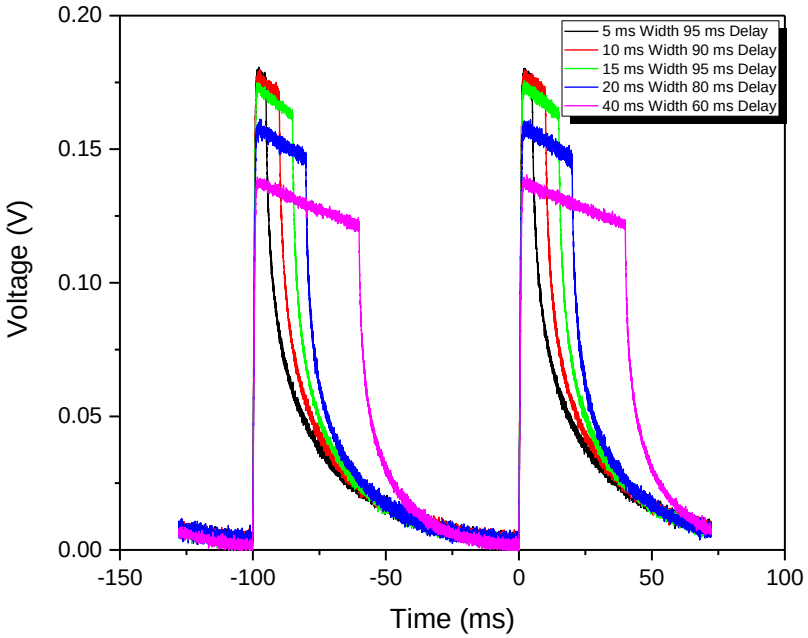

Figure 3.10: Time response of Si-GFET with fixed input power and different width/period ratio.

As the width increases from 5 ms to 40 ms the ratio width/period increases as a result the power on device also increases (Figure 2.12). It is expected that, regardless of the power applied, the peak value of the signal should remain constant. However, Figure 3.10 illustrates that when the device is exposed to power for more than 10 ms, the signal peak begins to decrease.It suggests that with a fixed pulse duration, increasing the width (ON time) of the device allows less time for the signal to fully decay. As a result, if light is applied again before the signal has completely decayed, the device, despite receiving higher power with an increased width, will show a reduced maximum signal. To address this issue, we set the width-to-period ratio to approximately 1/20. For instance, with a 100 ms pulse, the device is exposed to light for 5 ms and remains in darkness for the remaining 95 ms, resulting in a width-to-period ratio of 1/20.

3.8.2 Time Response with Change of Power

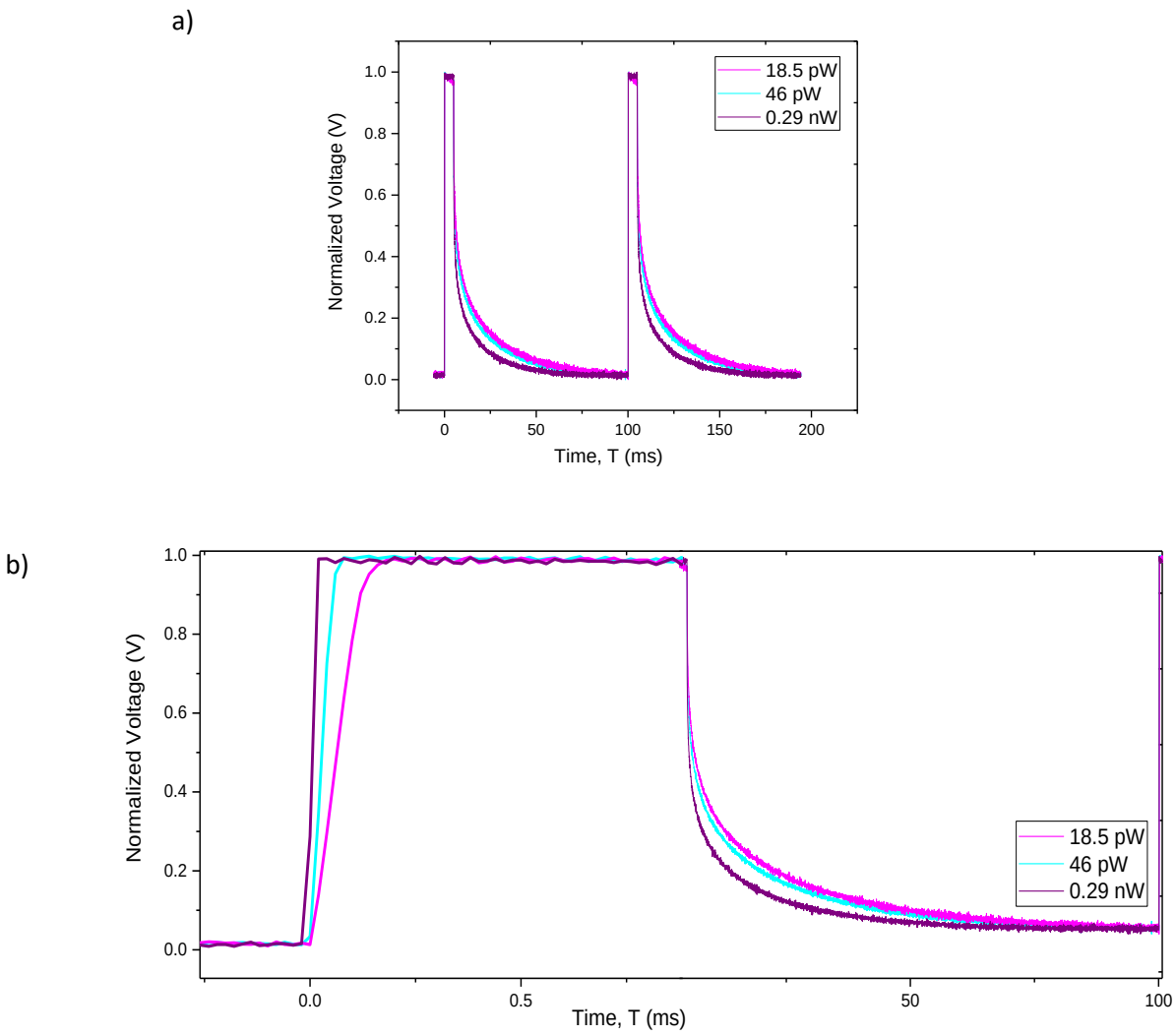

Figure 3.11: Time response characteristics with change of power using 532 nm light source. (a) Characteristic curve of normalized voltage vs time with 100 ms pulse and different power. (b) Zooming in figure (a) to show the slope of signal changing with increasing power.

Figure 3.11 shows the normalized signal in response to the change of power on device. Here, the pulse width is fixed to 100 ms and the width/period ratio is 1/20. Keeping the width/period fixed when we change the input power through half wave plate or neutral density filters the slope of the normalized signal starts to change.

3.8.3 Decay Time Response with Power

Figure 3.12 shows the change of decay time with increasing power from 57 fW to 0.37 nW. The decay time can be found using,

$$I_{ph} = A_1 \exp\left(-\frac{t}{\tau_{decay1}}\right) + A_2 \exp\left(-\frac{t}{\tau_{decay2}}\right) \quad (3.2)$$

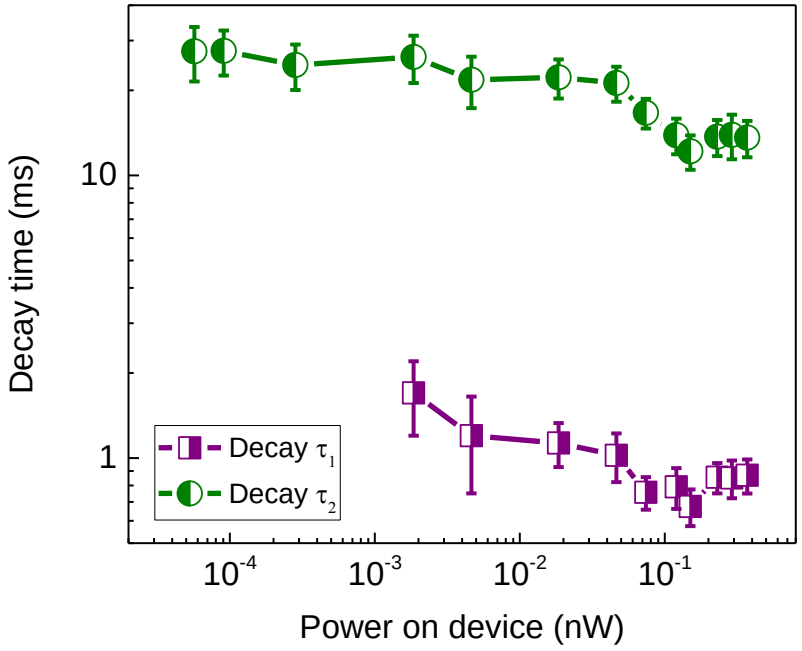

Figure 3.12: Decay time of GFET on Si substrate with power from 57 fW to 0.37 nW with V_{DS} =0.2 V, V_{BG}=-2 V and 532 nm light. The time response for high power shows two components τ_1 and τ_2 and for low power below 1.85 pW shows one decay component.

The decay time fitting reveals two components at high power and a single component at low power. Specifically, for the low power of 0.37 nW, the fast component has a decay time of 860 µs, while the slow component is 13.6 ms. These time response measurements indicate that the decay time is influenced by the carrier lifetime, which is strongly affected by the illumination power.

The slow component is observable at both low and high power levels. At low power levels, below 1.85 pW, electrons and holes are well-separated. When the light is turned off, it takes a long time for the electrons to escape from trapped centers, corresponding to the slow component of the decay time.

The fast component is observed only under high-power excitation. At high power levels, a greater number of electrons become trapped at the substrate/insulator interface. When the power is turned off, many electron-hole pairs undergo processes such as Auger non-radiative recombination and thermal excitation, which help remove trapped carriers from the interface potential. This significantly reduces the decay time, resulting in a faster response time. For high-power excitation, the fast component has a decay time of approximately 860 µs, while the slow component remains around ~14 ms.

3.8.4 Rise Time Response with Power

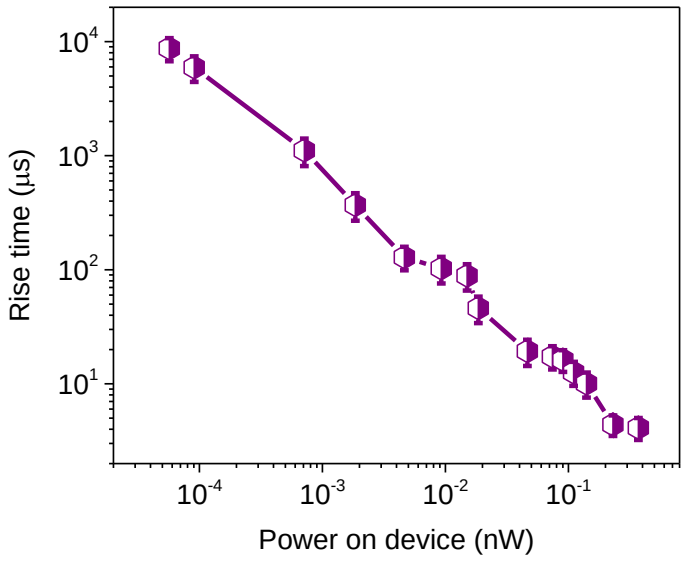

Figure 3.13: Rise time of GFET on Si substrate with power from 57 fW to 0.37 nW with V_{DS} = 0.2 V, V_{BG}=-2 V and 532 nm light.

In a similar way, the rise time component for each power can be found by fitting the equation,

$$I_{ph} = I_0 - A_1 \exp\left(-\frac{t}{\tau_1}\right) \quad \text{..... (3.3)}$$

The fitting indicates that the rise time consists of a single component across all power levels. It also shows that rise time decreases significantly with increasing power. At high power excitation, the rise time becomes thousands of times shorter compared to lower power levels. This suggests that at high power excitation, photogenerated carriers are created rapidly and transfer in the potential well much faster compared to lower power levels.

Chapter 4

Conclusion

In summary, we have systematically measured key parameters to evaluate the performance of GFET photodetectors fabricated on two different substrates, namely Si and GaAs. The substrates chosen for the device fabrication have a bandgap energy of 1.12 eV and 1.43 eV, respectively.

The responsivity measurements at various wavelengths reveal a significant drop from 10^6 A/W for both GFETs on Si and GaAs substrates when the incident photon energy falls below the substrates' bandgap energy. This indicates that responsivity is highly dependent on the substrate material, with the photogating effect primarily arising from the substrate.

Beyond the bandgap energy, the GFET on GaAs can detect wavelengths up to 1000 nm, while the Si device can detect up to 1600 nm, with responsivity around 26 A/W. Both devices remain responsive to light above their respective bandgap energies due to the slight *p*-doping of the substrates.

The mobility of both GaAs-GFET and Si-GFET are of the same order. Although the GaAs substrate is supposed to have higher mobility than the Si substrate, the dielectric properties are different (Si_3N_4 and SiO_2). Therefore, the dielectric layer has a more significant impact on carrier mobility than the substrate material itself.

The gain and sensitivity for different wavelengths for both materials are found to be in the same order, with the parameters for GaAs-GFET being slightly larger. The NEP and D* values for both devices are also of the same order. The highest values of NEP and D* for both devices are 10^{-15} ($W/\sqrt{Hz}$) and 10^{12} (Jones), respectively, indicating a sensitive photodetection.

The time response for Si-GFET reveals that the response time is power-dependent. Under low-power illumination, the decay time exhibits a single component. However, at high-power excitation, the decay time includes two components, with the fast decay time occurring in the range of a few hundred microseconds. In contrast, the rise time is consistently a single component across all power levels. The fastest rise time, observed at 370 pW, is approximately 4 μs. Overall, the rise times are shorter than the decay times, indicating that the photogenerated carriers rise more quickly than they decay.

References:

1. Xu, Y., & Lin, Q. (2020). Photodetectors based on solution-processable semiconductors: Recent advances and perspectives. *Applied Physics Reviews*, *7*(1), 011315. https://doi.org/10.1063/1.5144840 .
2. Konstantatos, G. (2018). Current status and technological prospect of photodetectors based on two-dimensional materials. *Nature Communications*, *9*(1). https://doi.org/10.1038/s41467-018-07643-7.
3. Rogalski, A. (2023). Commentary on the Record-Breaking Performance of Low-Dimensional Solid Photodetectors. *ACS Photonics*, *10*(3), 647–653. https://doi.org/10.1021/acsphotonics.2c01672
4. Di Bartolomeo, A. (2016). Graphene Schottky diodes: An experimental review of the rectifying graphene/semiconductor heterojunction. *Physics Reports*, *606*, 1–58. https://doi.org/10.1016/j.physrep.2015.10.003
5. Rogalski, A., Kopytko, M., & Martyniuk, P. (2017). *Antimonide-based infrared detectors: A New Perspective*. SPIE-International Society for Optical Engineering.
6. Rogalski, A. (2019). Graphene-based materials in the infrared and terahertz detector families: a tutorial. *Advances in Optics and Photonics*, *11*(2), 314. https://doi.org/10.1364/aop.11.000314
7. Novoselov, K. S. (2004). Electric Field Effect in Atomically Thin Carbon Films. *Science*, *306*(5696), 666–669. https://doi.org/10.1126/science.1102896
8. Allen, M. J., Tung, V. C., & Kaner, R. B. (2010). Honeycomb Carbon: A Review of Graphene. *Chemical Reviews*, *110*(1), 132–145. https://doi.org/10.1021/cr900070d
9. Koppens, F. H. L., Mueller, T., Avouris, Ph., Ferrari, A. C., Vitiello, M. S., & Polini, M. (2014). Photodetectors based on graphene, other two-dimensional materials and hybrid systems. *Nature Nanotechnology*, *9*(10), 780–793. https://doi.org/10.1038/nnano.2014.215
10. Long, M., Wang, P., Fang, H., & Hu, W. (2018). Progress, Challenges, and Opportunities for 2D Material Based Photodetectors. *Advanced Functional Materials*, *29*(19), 1803807. https://doi.org/10.1002/adfm.201803807
11. Vicarelli, L., Vitiello, M. S., Coquillat, D., Lombardo, A., Ferrari, A. C., Knap, W., Polini, M., Pellegrini, V., & Tredicucci, A. (2012). Graphene field-effect transistors as room-temperature terahertz detectors. *Nature Materials*, *11*(10), 865–871. https://doi.org/10.1038/nmat3417

12. Akinwande, D., Huyghebaert, C., Wang, C.-H., Serna, M. I., Goossens, S., Li, L.-J., Wong, H.-S. . P., & Koppens, F. H. L. (2019). Graphene and two-dimensional materials for silicon technology. *Nature*, *573*(7775), 507–518. https://doi.org/10.1038/s41586-019-1573-9
13. Li, J., Liu, C., Chen, H., Guo, J., Zhang, M., & Dai, D. (2020). Hybrid silicon photonic devices with two-dimensional materials. *Nanophotonics*, *9*(8), 2295–2314. https://doi.org/10.1515/nanoph-2020-0093
14. Mak, K. F., Ju, L., Wang, F., & Heinz, T. F. (2012). Optical spectroscopy of graphene: From the far infrared to the ultraviolet. *Solid State Communications*, *152*(15), 1341–1349. https://doi.org/10.1016/j.ssc.2012.04.064
15. Cao, G., Wang, F., Peng, M., Shao, X., Yang, B., Hu, W., Li, X., Chen, J., Shan, Y., Wu, P., Hu, L., Liu, R., Gong, H., Cong, C., & Qiu, Z. (2020). Multicolor Broadband and Fast Photodetector Based on InGaAs–Insulator–Graphene Hybrid Heterostructure. *Advanced Electronic Materials*, *6*(3). https://doi.org/10.1002/aelm.201901007
16. Semenoff, G. W. (1984). Condensed-Matter Simulation of a Three-Dimensional Anomaly. *Physical Review Letters*, *53*(26), 2449–2452. https://doi.org/10.1103/physrevlett.53.2449
17. Wallace, P. R. (1947). The Band Theory of Graphite. *Physical Review*, *71*(9), 622–634. https://doi.org/10.1103/physrev.71.622
18. A. H. Castro Neto, Guinea, F., N. M. R. Peres, Novoselov, K. S., & Geim, A. K. (2009). The electronic properties of graphene. *Reviews of Modern Physics*, *81*(1), 109–162. https://doi.org/10.1103/revmodphys.81.109
19. Novoselov, K. S., Geim, A. K., Morozov, S. V., Jiang, D., Katsnelson, M. I., Grigorieva, I. V., Dubonos, S. V., & Firsov, A. A. (2005). Two-dimensional gas of massless Dirac fermions in graphene. *Nature*, *438*(7065), 197–200. https://doi.org/10.1038/nature04233
20. Geim, A. K., & Novoselov, K. S. (2007). The rise of graphene. *Nature Materials*, *6*(3), 183–191. https://doi.org/10.1038/nmat1849
21. Bolotin, K. I., Sikes, K. J., Jiang, Z., Klima, M., Fudenberg, G., Hone, J., Kim, P., & Stormer, H. L. (2008). Ultrahigh electron mobility in suspended graphene. *Solid State Communications*, *146*(9-10), 351–355. https://doi.org/10.1016/j.ssc.2008.02.024

22. Nathan, M. I., Dumke, W. P., K. Wrenner, Tiwari, S., Wright, S. L., & Jenkins, K. A. (1988). Electron mobility in *p*-type GaAs. *Applied Physics Letters*, *52*(8), 654–656. https://doi.org/10.1063/1.99395
23. Rode, D. L. (1971). Electron Transport in InSb, InAs, and InP. *Physical Review. B, Solid State*, *3*(10), 3287–3299. https://doi.org/10.1103/physrevb.3.3287
24. Xia, F. Yan, H. and Avouris, P. (2013) "The interaction of light and graphene: basic, devices, and applications," Proc. IEEE 101, 1717–1731.
25. Chen, J.-H., Jang, C., Xiao, S., Ishigami, M., & Fuhrer, M. S. (2008). Intrinsic and extrinsic performance limits of graphene devices on SiO2. *Nature Nanotechnology*, *3*(4), 206–209. https://doi.org/10.1038/nnano.2008.58
26. Zhang, Y., Mendez, E. E., & Du, X. (2011). Mobility-Dependent Low-Frequency Noise in Graphene Field-Effect Transistors. *ACS Nano*, *5*(10), 8124–8130. https://doi.org/10.1021/nn202749z
27. Gosling, J. H., Makarovsky, O., Wang, F., Cottam, N. D., Greenaway, M. T., Patanè, A., Wildman, R. D., Tuck, C. J., Turyanska, L., & Fromhold, T. M. (2021). Universal mobility characteristics of graphene originating from charge scattering by ionised impurities. *Communications Physics*, *4*(1), 1–8. https://doi.org/10.1038/s42005-021-00518-2
28. Zhong, B., Md Ahsan Uddin, Singh, A., Webb, R., & Koley, G. (2016). Temperature dependent carrier mobility in graphene: Effect of Pd nanoparticle functionalization and hydrogenation. *Applied Physics Letters*, *108*(9). https://doi.org/10.1063/1.4942975
29. Hirai, H., Tsuchiya, H., Kamakura, Y., Mori, N., & Ogawa, M. (2014). Electron mobility calculation for graphene on substrates. *Journal of Applied Physics*, *116*(8), 083703. https://doi.org/10.1063/1.4893650
30. Hong Ye Song, Li, S., Miyazaki, H., Sato, S., Hayashi, K., Yamada, A., Yokoyama, N., & Kazuhito Tsukagoshi. (2012). *Origin of the relatively low transport mobility of graphene grown through chemical vapor deposition*. *2*(1). https://doi.org/10.1038/srep00337
31. Wang, J., Hernandez, Y., Lotya, M., Coleman, J. N., & Blau, W. J. (2009). Broadband Nonlinear Optical Response of Graphene Dispersions. *Advanced Materials*, *21*(23), 2430–2435. https://doi.org/10.1002/adma.200803616

32. Mak, K. F., Ju, L., Wang, F., & Heinz, T. F. (2012). Optical spectroscopy of graphene: From the far infrared to the ultraviolet. *Solid State Communications*, *152*(15), 1341–1349. https://doi.org/10.1016/j.ssc.2012.04.064
33. Nair, R. R., Blake, P., Grigorenko, A. N., Novoselov, K. S., Booth, T. J., Stauber, T., Peres, N. M. R., & Geim, A. K. (2008). Fine Structure Constant Defines Visual Transparency of Graphene. *Science*, *320*(5881), 1308–1308. https://doi.org/10.1126/science.1156965
34. Stauber, T., Peres, N. M. R., & Geim, A. K. (2008). Optical conductivity of graphene in the visible region of the spectrum. *Physical Review B*, *78*(8). https://doi.org/10.1103/physrevb.78.085432
35. Wang, F., Zhang, Y., Tian, C., Girit, C., Zettl, A., Crommie, M., & Shen, Y. R. (2008). Gate-Variable Optical Transitions in Graphene. *Science*, *320*(5873), 206–209. https://doi.org/10.1126/science.1152793
36. Furchi, M., Urich, A., Pospischil, A., Lilley, G., Unterrainer, K., Detz, H., Klang, P., Andrews, A. M., Schrenk, W., Strasser, G., & Mueller, T. (2012). Microcavity-Integrated Graphene Photodetector. *Nano Letters*, *12*(6), 2773–2777. https://doi.org/10.1021/nl204512x
37. Wei Lien Wang, Andrey Klots, Yang, Y., Li, W., Kravchenko, I. I., Briggs, D. P., Bolotin, K. I., & Valentine, J. (2015). *Enhanced absorption in two-dimensional materials via Fano-resonant photonic crystals*. *106*(18), 181104–181104. https://doi.org/10.1063/1.4919760
38. Xia, F., Wang, H., Xiao, D., Dubey, M. & Ramasubramaniam, A. (2014). Twodimensional material nanophotonics. Nature Photonics 8, 899–907.
39. Bao, Q. & Loh, K. P. (2012). Graphene Photonics, Plasmonics, and Broadband Optoelectronic Devices. ACS Nano 6, 3677–3694.
40. Eda, G. & Maier, S. A. (2013). Two-Dimensional Crystals: Managing Light for Optoelectronics. ACS Nano 7, 5660–5665.
41. Low, T. and Avouris, P. (2014) "Graphene plasmonic for terahertz to mid-infrared applications," ACS Nano 8, 1086–1101.
42. Park, J., Ahn, Y. H., & Ruiz-Vargas, C. (2009). Imaging of Photocurrent Generation and Collection in Single-Layer Graphene. *Nano Letters*, *9*(5), 1742–1746. https://doi.org/10.1021/nl8029493
43. Xia, F. N.; Mueller, T.; Lin, Y. M.; Valdes-Garcia, A.; Avouris, P. (2009) Ultrafast graphene photodetector. Nat. Nanotechnol. 4, 839−843.

44. Xia, F. N.; Mueller, T.; Golizadeh-Mojarad, R.; Freitag, M.; Lin, Y. M.; Tsang, J.; Perebeinos, V.; Avouris, P. (2009) Photocurrent Imaging and Efficient Photon Detection in a Graphene Transistor. Nano Lett. 9, 1039−1044.
45. Lemme, M. C.; Koppens, F. H. L.; Falk, A. L.; Rudner, M. S.; Park, H.; Levitov, L. S.; Marcus, C. M. (2011). Gate-Activated Photoresponse in a Graphene p-n Junction. Nano Lett. 11, 4134−4137.
46. Ho, V. X., Wang, Y., Howe, L., Cooney, M. P., & Vinh, N. Q. (2022). Shallow Impurity States in Doped Silicon Substrates Enabling High Responsivity for Graphene Mid-Infrared Photodetectors. *ACS Applied Nano Materials*, *5*(9), 12477–12486. https://doi.org/10.1021/acsanm.2c02011
47. Guo, W., Xu, S., Wu, Z., Wang, N., Loy, M. M. T., & Du, S. (2013). Oxygen-Assisted Charge Transfer Between ZnO Quantum Dots and Graphene. *Small*, *9*(18), 3031–3036. https://doi.org/10.1002/smll.201202855
48. Boruah, B. D., & Misra, A. (2015). ZnO quantum dots and graphene based heterostructure for excellent photoelastic and highly sensitive ultraviolet photodetector. *RSC Advances*, *5*(110), 90838–90846. https://doi.org/10.1039/c5ra18663c
49. Vincent JD. (2016).Fundamentals of infrared and visible detector operation and testing, Second edition. edn. Wiley.
50. Saleh BEA, Teich MC. (2007). Fundamentals of photonics, 2nd edn. Wiley Interscience.
51. Balandin, A.A., (2002) Noise and Fluctuations Control in Electronic Devices, American Scientific Publishers.
52. Richards, P.L. (1994). "Bolometers for infrared and millimeter waves," Journal of Applied Physics 76, (1) https://doi:10.1063/1.357128
53. Balandin, A.A., (2013). Low-frequency 1/f noise in graphene devices. Nat. Nanotechnol.,. 8 (549).
54. Kayyalha, M., & Chen, Y. P. (2015). Observation of reduced 1/f noise in graphene field effect transistors on boron nitride substrates. *Applied Physics Letters*, *107*(11), 113101. https://doi.org/10.1063/1.4930992
55. Rumyantsev, S., Liu, G., Stillman, W., Shur, M., & Balandin, A. A. (2010). Electrical and noise characteristics of graphene field-effect transistors: ambient effects, noise sources and

physical mechanisms. *Journal of Physics: Condensed Matter*, *22*(39), 395302. https://doi.org/10.1088/0953-8984/22/39/395302

56. Lin, Y.-M., & Phaedon Avouris. (2008). *Strong Suppression of Electrical Noise in Bilayer Graphene Nanodevices*. *8*(8), 2119–2125 https://doi.org/10.1021/nl0802411
57. El-Desouki, M., Jamal Deen, M., Fang, Q., Liu, L., Tse, F., & Armstrong, D. (2009). CMOS Image Sensors for High Speed Applications. *Sensors*, *9*(1), 430–444. https://doi.org/10.3390/s90100430
58. None Bin Luo, None Fuxing Yang, & None Lei Yan. (2010). *Key technologies and research development of CMOS image sensors*. https://doi.org/10.1109/iita-grs.2010.5602944
59. Huo., N. Konstantatos, G. (2018). Recent progress and future prospects of 2D-based photodetectors, Adv. Mater. 30(51), 1801164.
60. Feiginov, M. N. (2007). Analysis of limitations of terahertz p-i-n uni-traveling-carrier photodiodes. *Journal of Applied Physics*, *102*(8), 084510. https://doi.org/10.1063/1.2801400
61. Konstantatos, G., Howard, I., Fischer, A., Hoogland, S., Clifford, J., Klem, E., Levina, L., & Sargent, E. H. (2006). Ultrasensitive solution-cast quantum dot photodetectors. *Nature*, *442*(7099), 180–183. https://doi.org/10.1038/nature04855
62. Clifford, J. P. Konstantatos, G. Johnston, K. W. Hoogland, S. Levina, L. Sargent., E. H. (2009) Fast, sensitive and spectrally tuneable colloidal-quantum-dot photodetectors. Nat. Nanotechnol. 4 (40).
63. Anupam Chetia, Jayanta Bera, Atanu Betal, Satyajit Sahu, (2022) A brief review on photodetector performance based on zero dimensional and two-dimensional materials and their hybrid structures, Materials Today Communications, Volume 30, 103224, ISSN 2352-4928, https://doi.org/10.1016/j.mtcomm.2022.103224.
64. Jung, P.-G., Oh, J.-M., Kim, N.-H., & Abdelkader Abderrahmane. (2020). Optoelectronic properties of two-dimensional molybdenum diselenide dual-gated MISFET-based photodetector. *Optik*, *224*, 165427–165427. https://doi.org/10.1016/j.ijleo.2020.165427
65. Liu, Y., Cheng, R., Liao, L., Zhou, H., Bai, J., Liu, G., Liu, L., Huang, Y., & Duan, X. (2011). Plasmon resonance enhanced multicolour photodetection by graphene. *Nature Communications*, *2*(1). https://doi.org/10.1038/ncomms1589
66. Tan, Z., Wu, Y., Hong, H., Yin, J., Zhang, J., Lin, L., Wang, M., Xiao Wei Sun, Sun, L., Huang, Y., Liu, K., Liu, Z., & Peng, H. (2016). Two-Dimensional

($C_4H_9NH_3)_2PbBr_4$ Perovskite Crystals for High-Performance Photodetector. *Journal of the American Chemical Society*, *138*(51), 16612–16615. https://doi.org/10.1021/jacs.6b11683

67. Sun, Z., Liu, Z., Li, J., Tai, G., Lau, S.-P., & Yan, F. (2012). Infrared Photodetectors Based on CVD-Grown Graphene and PbS Quantum Dots with Ultrahigh Responsivity. *Advanced Materials*, *24*(43), 5878–5883. https://doi.org/10.1002/adma.201202220
68. Konstantatos, G., Badioli, M., Gaudreau, L., Osmond, J., Bernechea, M., de Arquer, F. P. G., Gatti, F., & Koppens, F. H. L. (2012). Hybrid graphene–quantum dot phototransistors with ultrahigh gain. *Nature Nanotechnology*, *7*(6), 363–368. https://doi.org/10.1038/nnano.2012.60
69. Liu, Q., Tian, H., Li, J., Hu, A., He, X., Sui, M., & Guo, X. (2019). Hybrid Graphene/Cu $_2$ O Quantum Dot Photodetectors with Ultrahigh Responsivity. *Advanced Optical Materials*, *7*(20), 1900455. https://doi.org/10.1002/adom.201900455

70. Tetsuka, H. (2017). 2D/0D graphene hybrids for visible-blind flexible UV photodetectors. *Scientific Reports*, *7*(1). https://doi.org/10.1038/s41598-017-05981-y
71. Yu, W., Li, S., Zhang, Y., Ma, W., Sun, T., Yuan, J., Fu, K., & Bao, Q. (2017). Near-Infrared Photodetectors Based on MoTe2 /Graphene Heterostructure with High Responsivity and Flexibility. *Small*, *13*(24), 1700268. https://doi.org/10.1002/smll.201700268
72. Liu, Y., Shivananju, B. N., Wang, Y., Zhang, Y., Yu, W., Xiao, S., Sun, T., Ma, W., Mu, H., Lin, S., Zhang, H., Lu, Y., Qiu, C.-W., Li, S., & Bao, Q. (2017). Highly Efficient and Air-Stable Infrared Photodetector Based on 2D Layered Graphene–Black Phosphorus Heterostructure. *ACS Applied Materials & Interfaces*, *9*(41), 36137–36145. https://doi.org/10.1021/acsami.7b09889
73. Roy, K., Padmanabhan, M., Goswami, S., Sai, T. P., Ramalingam, G., Raghavan, S., & Ghosh, A. (2013). Graphene–MoS2 hybrid structures for multifunctional photoresponsive memory devices. *Nature Nanotechnology*, *8*(11), 826–830. https://doi.org/10.1038/nnano.2013.206
74. Chang, P.-L., Liu, S., Lan, Y.-B., Tsai, Y.-C., You, X.-Q., Li, C.-S., Huang, K.-C., Chou, A.-S., Cheng, T.-C., & Wang, J.-K. (2017). Ultrahigh Responsivity and Detectivity Graphene–Perovskite Hybrid Phototransistors by Sequential Vapor Deposition. *Scientific Reports*, *7*(1). https://doi.org/10.1038/srep46281

75. An, X., Liu, F., Jung, Y. J., & Kar, S. (2013). Tunable Graphene–Silicon Heterojunctions for Ultrasensitive Photodetection. *Nano Letters*, *13*(3), 909–916. https://doi.org/10.1021/nl303682j
76. Park H.-K. and Choi J. (2018). High responsivity and detectivity graphene-silicon majority carrier tunneling photodiodes with a thin native oxide layer ACS Photonics 5 2895.
77. Xu J.-Y., Yu J.-S., Liao J.-H., Yang X.-B., Wu C.-Y., Wang Y., Wang L., Xie C. and Luo L.-B. (2019). Opening the band gap of Graphene via fluorination for high-performance dual-mode photodetector application ACS Appl. Mater. Interfaces 11 21702.
78. Li X. et al. (2016). High detectivity graphene-silicon heterojunction photodetector Small 12 595.
79. Wu J., Lu Y., Feng S., Wu Z., Lin S., Hao Z., Yao T., Li X., Zhu H. and Lin S. (2018). The Interaction between quantum dots and Graphene: the applications in Graphene-based solar cells and photodetectors Adv. Funct. Mater. 28 1804712.
80. Wang, Y., Ho, V. X., Pradhan, P., Cooney, M. P., & Vinh, N. Q. (2021). Interfacial Photogating Effect for Hybrid Graphene-Based Photodetectors. *ACS Applied Nano Materials*, *4*(8), 8539–8545. https://doi.org/10.1021/acsanm.1c01931
81. Zhang, Y. B.; Brar, V. W.; Girit, C.; Zettl, A.; Crommie, M. F.(2009). Origin of spatial charge inhomogeneity in graphene. Nat. Phys. 5, 722−726.
82. Hollander, M. J.; LaBella, M.; Hughes, Z. R.; Zhu, M.; Trumbull, K. A.; Cavalero, R.; Snyder, D. W.; Wang, X. J.; Hwang, E.; Datta, S.; Robinson, J. A. (2011). Enhanced Transport and Transistor Performance with Oxide Seeded High-kappa Gate Dielectrics on Wafer-Scale Epitaxial Graphene. Nano Lett. 11, 3601−3607.
83. Bidmeshkipour, S. Vorobiev, A. Andersson, M. A. Kompany, A. & Stake, J. (2015). Effect of ferroelectric substrate on carrier mobility in graphene field-effect transistors. *Applied Physics Letters*, *107*(17). https://doi.org/10.1063/1.4934696
84. Fang, C., Xia, J., Ferry, D. K., & Tao, N. (2009). Dielectric Screening Enhanced Performance in Graphene FET. *Nano Letters*, *9*(7), 2571–2574. https://doi.org/10.1021/nl900725u
85. Gao, L., Ren, W., Xu, H., Li, J., Wang, Z., Ma, T., Peng, L., Zhang, Z., Fu, Q., Peng, L., Bao, X., & Cheng, H.-M. (2012). *Repeated growth and bubbling transfer of graphene with millimetre-size single-crystal grains using platinum*. *3*(1). https://doi.org/10.1038/ncomms1702

86. Wang, X., Hao, Z., Olsen, T. R., Zhang, W., & Lin, Q. (2019). Measurements of aptamer–protein binding kinetics using graphene field-effect transistors. *Nanoscale*, *11*(26), 12573–12581. https://doi.org/10.1039/c9nr02797a
87. Fukushima, S., Masaaki Shimatani, Okuda, S., Ogawa, S., Kanai, Y., Ono, T., Inoue, K., & Matsumoto, K. (2019). Low dark current and high-responsivity graphene mid-infrared photodetectors using amplification of injected photo-carriers by photo-gating. *Optics Letters/Optics Index*, *44*(10), 2598–2598. https://doi.org/10.1364/ol.44.002598
88. Okamoto, S., Ohno, Y., Kenzo Maehashi, Inoue, K., & Matsumoto, K. (2012). Immunosensors Based on Graphene Field-Effect Transistors Fabricated Using Antigen-Binding Fragment. *Japanese Journal of Applied Physics*, *51*(6S), 06FD08–06FD08. https://doi.org/10.7567/jjap.51.06fd08
89. Fu, W., Jiang, L., van Geest, E. P., Lima, L. M. C., & Schneider, G. F. (2016). Sensing at the Surface of Graphene Field-Effect Transistors. *Advanced Materials*, *29*(6), 1603610. https://doi.org/10.1002/adma.201603610
90. Morgan, D. V.; Board, K. (1991). An Introduction To Semiconductor Microtechnology (2nd ed.). Chichester, West Sussex, England: John Wiley & Sons. p. 137. ISBN 978-0471924784.
91. O'Connor, E., Brennan, B., Vladimir Djara, Karim Cherkaoui, Monaghan, S., Newcomb, S. B., Contreras, R., Marko Milojević, Hughes, G., Pemble, M. E., Wallace, R. M., & Hurley, P. K. (2011). A systematic study of (NH4)2S passivation (22%, 10%, 5%, or 1%) on the interface properties of the Al2O3/In0.53Ga0.47As/InP system for n-type and p-type In0.53Ga0.47As epitaxial layers. *Journal of Applied Physics*, *109*(2). https://doi.org/10.1063/1.3533959
92. Zhu, Y., Chen, X., Ma, Y., Zhang, Y., Du, B., Shi, Y., & Gu, Y. (2018). Surface and optical properties of silicon nitride deposited by inductively coupled plasma-chemical vapor deposition. *Journal of Semiconductors/Journal of Semiconductors*, *39*(8), 083005–083005. https://doi.org/10.1088/1674-4926/39/8/083005
93. Kaloyeros, A. E., Jové, F. A., Goff, J., & Arkles, B. (2017). Review—Silicon Nitride and Silicon Nitride-Rich Thin Film Technologies: Trends in Deposition Techniques and Related Applications. *ECS Journal of Solid State Science and Technology*, *6*(10), P691–P714. https://doi.org/10.1149/2.0011710jss

94. Igor Krylov, Gavrilov, A., Ritter, D., & Eizenberg, M. (2011). Elimination of the weak inversion hump in Si3N4/InGaAs (001) gate stacks using an *in situ* NH3 pre-treatment. *Applied Physics Letters*, *99*(20). https://doi.org/10.1063/1.3662035
95. Shu-Yan, Z. *et al.* (2013). Improved interface properties of an HfO_2 gate dielectric GaAs MOS device by using SiN_x as an interfacial passivation layer. Chinese Physics B.
96. Eamon O'Connor, Vladimir Djara, Monaghan, S., Hurley, P., & Karim Cherkaoui. (2011). Capacitance-Voltage and Interface State Density Characteristics of GaAs and $In_{0.53}Ga_{0.47}As$ MOS Capacitors Incorporating a PECVD Si_3N_4 Dielectric. *ECS Transactions*, *35*(3), 415–430. https://doi.org/10.1149/1.3569934
97. Headley, C., Fu, L., Parkinson, P., Xu, X., Lloyd-Hughes, J., Chennupati Jagadish, & Johnston, M. B. (2011). Improved Performance of GaAs-Based Terahertz Emitters via Surface Passivation and Silicon Nitride Encapsulation. *IEEE Journal of Selected Topics in Quantum Electronics*, *17*(1), 17–21. https://doi.org/10.1109/jstqe.2010.2047006
98. Diao, Y., Liu, L., & Xia, S. (2019). Exploration the p-type doping mechanism of GaAs nanowires from first-principles study. *Physics Letters. A*, *383*(2-3), 202–209. https://doi.org/10.1016/j.physleta.2018.10.037
99. Tan, Y.-W., Zhang, Y., Bolotin, K. I., Zhao, Y., Adam, S., Hwang, E. H., S. Das Sarma, Stormer, H. L., & Kim, P. (2007). Measurement of Scattering Rate and Minimum Conductivity in Graphene. *Physical Review Letters*, *99*(24). https://doi.org/10.1103/physrevlett.99.246803
100. Ando, T. (2006). Screening Effect and Impurity Scattering in Monolayer Graphene. *Journal of the Physical Society of Japan*, *75*(7), 074716. https://doi.org/10.1143/jpsj.75.074716
101. Yu, Q., Jauregui, L. A., Wu, W., Colby, R., Tian, J., Su, Z., Cao, H., Liu, Z., Pandey, D., Wei, D., Chung, T. F., Peng, P., Guisinger, N. P., Stach, E. A., Bao, J., Pei, S.-S., & Chen, Y. P. (2011). Control and characterization of individual grains and grain boundaries in graphene grown by chemical vapour deposition. *Nature Materials*, *10*(6), 443–449. https://doi.org/10.1038/nmat3010
102. Cao, H., Yu, Q., Colby, R. J., Pandey, D., Park, C. S., Lian, J., Dmitry Zemlyanov, Childres, I., Drachev, V. P., Stach, E. A., Muhammad Mustafa Hussain, Li, H., Pei, S., & Chen, Y. (2010). Large-scale graphitic thin films synthesized on Ni and transferred to insulators:

Structural and electronic properties. *Journal of Applied Physics*, *107*(4), 044310–044310. https://doi.org/10.1063/1.3309018

103. Cao, H., Yu, Q., Jauregui, L. A., Tian, J., Wu, W., Liu, Z., Romaneh Jalilian, Benjamin, D. K., Jiang, Z., Bao, J., Pei, S., & Chen, Y. (2009). *Electronic transport in chemical vapor deposited graphene synthesized on Cu: Quantum Hall effect and weak localization*. *96*(12), 122106–122106. https://doi.org/10.1063/1.3371684

104. Adam, S., Hwang, E. H., & S. Das Sarma. (2008). Scattering mechanisms and Boltzmann transport in graphene. *Physica E Low-Dimensional Systems and Nanostructures*, *40*(5), 1022–1025. https://doi.org/10.1016/j.physe.2007.09.064

105. Zhu, W., Perebeinos, V., Freitag, M., & Avouris, P. (2009). Carrier scattering, mobilities, and electrostatic potential in monolayer, bilayer, and trilayer graphene. *Physical Review B*, *80*(23). https://doi.org/10.1103/physrevb.80.235402

106. Zhang, Z., Xu, H., Zhong, H., & Peng, L.-M. (2012). Direct extraction of carrier mobility in graphene field-effect transistor using current-voltage and capacitance-voltage measurements. *Applied Physics Letters*, *101*(21), 213103. https://doi.org/10.1063/1.4768690

107. Szafranek, B. N., Fiori, G., Schall, D., Neumaier, D., & Kurz, H. (2012). Current Saturation and Voltage Gain in Bilayer Graphene Field Effect Transistors. *Nano Letters*, *12*(3), 1324–1328. https://doi.org/10.1021/nl2038634

Lin, Y.-M., Jenkins, K. A., Valdes-Garcia, A., Small, J. P., Farmer, D. B., & Avouris, P. (2009). Operation of Graphene Transistors at Gigahertz Frequencies. *Nano Letters*, *9*(1), 422–426. https://doi.org/10.1021/nl803316h

108. Berdebes, D., Low, T., Sui, Y., Appenzeller, J., & Lundstrom, M. S. (2011). Substrate Gating of Contact Resistance in Graphene Transistors. *IEEE Transactions on Electron Devices*, *58*(11), 3925–3932. https://doi.org/10.1109/ted.2011.2163800

109. Petrone, N., Meric, I., Hone, J., & Shepard, K. L. (2012). Graphene Field-Effect Transistors with Gigahertz-Frequency Power Gain on Flexible Substrates. *Nano Letters*, *13*(1), 121–125. https://doi.org/10.1021/nl303666m

110. Wang, Y., et al., (2021). Effect of High-K Dielectric Layer on 1/f Noise Behavior in Graphene Field Effect Transistors. ACS Applied Nano Materials. 4: p. 3647-36.

111. Min-Kyu Kim, W.-H.K., Taeyoon Lee, Hyungjun Kim, (2013). Growth characteristics and electrical properties of Ta_2O_5grown bythermal and O_3-based atomic layer deposition on TiN substrates for metal–insulator–metalcapacitor applications. Thin Solid Films, 542: p. 71-75.

112. Lu, Q., Park, D., A. Kalnitsky, Chang, C., Cheng, C.-C., Sing Pin Tay, King, T.-J., & Hu, C. (1998). Leakage current comparison between ultra-thin Ta_2O_5 films and conventional gate dielectrics. *IEEE Electron Device Letters*, *19*(9), 341–342. https://doi.org/10.1109/55.709635

113. B. Raeissi, J. Piscator, Engstrom, O., Hall, S., O. Buiu, Lemme, M. C., Gottlob, B., Hurley, P. K., K. Cherkaoui, & Osten, H. J. (2007). *High-k-oxide/silicon interfaces characterized by capacitance frequency spectroscopy*. https://doi.org/10.1109/essderc.2007.4430933

114. Sun, S. C., & Chen, T. F. (1996). Leakage current reduction in chemical-vapor-deposited Ta_2O_5 films by rapid thermal annealing in N_2O. *IEEE Electron Device Letters*, *17*(7), 355–357. https://doi.org/10.1109/55.506365

115. Maria Letizia Terranova, Guglielmotti, V., Orlanducci, S., Sessa, V., Tamburri, E., & Rossi, M. (2009). Preparation and Functional Characterizations of Ta2O5 Deposits Organized at the Micro- and Nanoscale. *Meeting Abstracts/Meeting Abstracts (Electrochemical Society. CD-ROM)*, *MA2009-02*(34), 2645–2645. https://doi.org/10.1149/ma2009-02/34/2645

116. E. Atanassova, T. Dimitrova, H.S. Nalva (Ed.), (2001). Chapter 9 - THIN Ta2O5 LAYERS ON Si AS AN ALTERNATIVE TO SiO2 FOR HIGH-DENSITY DRAM APPLICATIONS. Handbook of Surfaces and Interfaces of Materials, vol. 4, Academic Press , San Diego, USA, p. 439.

117. C. Chaneliere, J.L. Autran, R.A.B. (1999). Devine Conduction mechanisms in Ta_2O_5/SiO_2 and Ta_2O_5/Si_3N_4 stacked structures on Si. J. Appl. Phys., 86 (480).

118. E. Atanassova, D. Spassov, & A. Paskaleva. (2006). Influence of the metal electrode on the characteristics of thermal Ta2O5 capacitors. *Microelectronic Engineering*, *83*(10), 1918–1926. https://doi.org/10.1016/j.mee.2006.01.043

119. Christensen, C., Roger de Reus, & Siebe Bouwstra. (1999). Tantalum oxide thin films as protective coatings for sensors. *Journal of Micromechanics and Microengineering*, *9*(2), 113–118. https://doi.org/10.1088/0960-1317/9/2/003

120. Kim, H. (2003). Atomic layer deposition of metal and nitride thin films: Current research efforts and applications for semiconductor device processing. *Journal of Vacuum Science & Technology*, *21*(6), 2231–2261. https://doi.org/10.1116/1.1622676

121. Kim, H., Lee, H.-B.-R., & Maeng, W.-J. . (2009). Applications of atomic layer deposition to nanofabrication and emerging nanodevices. *Thin Solid Films*, *517*(8), 2563–2580. https://doi.org/10.1016/j.tsf.2008.09.007

122. H. Demiryont, Sites, J. R., & Geib, K. (1985). Effects of oxygen content on the optical properties of tantalum oxide films deposited by ion-beam sputtering. *Applied Optics*, *24*(4), 490–490. https://doi.org/10.1364/ao.24.000490

123. Venugopal, A., Chan, J., Li, X., Magnuson, C. W., Kirk, W. P., Colombo, L., Ruoff, R. S., & Vogel, E. M. (2011). Effective mobility of single-layer graphene transistors as a function of channel dimensions. *Journal of Applied Physics*, *109*(10). https://doi.org/10.1063/1.3592338

124. Kim, S., Nah, J., Jo, I., Davood Shahrjerdi, Colombo, L., Yao, Z., Tutuc, E., & Banerjee, S. K. (2009). Realization of a high mobility dual-gated graphene field-effect transistor with Al2O3 dielectric. *Applied Physics Letters*, *94*(6), 062107–062107. https://doi.org/10.1063/1.3077021

125. Rambadey, O. V., Kumar, A., Aanchal Sati, & Sagdeo, P. R. (2021). Exploring the Interrelation between Urbach Energy and Dielectric Constant in Hf-Substituted $BaTiO_3$. *ACS Omega*, *6*(47), 32231–32238. https://doi.org/10.1021/acsomega.1c05057

126. Vinh X. Ho, Yifei Wang, Michael P. Cooneyb and N. Q. Vinh. (2021). Graphene-Ta_2O_5 heterostructure enabled high performance, deep-ultraviolet to mid-infrared photodetection Nanoscale, 13, 10526.

127. Rut'kov, E. V., Afanas'eva, E. Y., & Gall, N. R. (2020). Graphene and graphite work function depending on layer number on Re. *Diamond and Related Materials*, *101*, 107576. https://doi.org/10.1016/j.diamond.2019.107576

128. Novikov, A. (2010). Experimental measurement of work function in doped silicon surfaces. *Solid-State Electronics*, *54*(1), 8–13. https://doi.org/10.1016/j.sse.2009.09.005